EVALUATION OF THE POROSITY DISTRIBUTION IN LOST-FOAM CAST ALUMINUM SILICON 319 ALLOY THROUGH DESTRUCTIVE AND NON-DESTRUCTIVE METHODS

BY

KATHLEEN SACHIKO HOLLOWAY

B.S., University of Illinois, 1988

THESIS

submitted in partial fulfillment of the requirements
for the degree of Master of Science in Material Science and Engineering
in the Graduate College of the
University of Illinois at Urbana-Champaign, 1989

Urbana, Illinois

ABSTRACT

Porous defects within lost-foam cast aluminum-silicon 319 alloy have a detrimental effect on fatigue properties. Non-destructive and destructive techniques were used to study the nature of the pores and their distribution in the alloy. The performance of the non-destructive techniques, radiography and acoustic microscopy, were evaluated by comparing these results to the destructive evaluation results from fatigue fractured samples and polished sections. In addition, ultrasonic testing was investigated as a non-destructive technique.

The pores had irregular disk shapes and were randomly orientated. The distributions from the largest dimensions; (2C), (L), and radiographic measurements had similar gamma relationships with a coefficient between 1 and 2. However, a function governing the critical dimension (a) of the pores initiating fatigue failure was not apparent. Destructive tests validated the capability of the non-destructive techniques to identify pores.

ACKNOWLEDGEMENTS

This investigation was conducted in the Newmark Civil Engineering Laboratory, Department of Civil Engineering, at the University of Illinois, Urbana. The program was funded by the General Motors Technical Center, Warren, Michigan under the guidance of Mr. Richard Osbourne and Dr. Dale Gerald.

I would like to express my sincere appreciation to Dr. Frederick V. Lawrence, Jr. for his guidance with my masters thesis.

Dr. William O'Brien and his research group are gratefully acknowledged for their suggestions and assistance with this thesis. Ms. Wendy Crone is thanked for her invaluable assistance and patience with the SLAM.

Dr. T.J. Rowland is acknowledged for allowing me to use the Quantimet and for his help with it.

Gratitude is extended to Dr. Grzegroz Banas and Dr. Henrique Reis for their valuable suggestions with this thesis. Mr. Michael Conlon, Mr. Charles Kurnik and Ms. Jill Oderio each made important contributions in the preparation of samples and microscopy work.

Mr. Anthony J. Biell IV, Mr. Mohammed H. Swellam and Mr. Chih-Hsien Ting, my colleagues and friends, are each recognized for their technical expertise as well as for their humor which made each passing day a little brighter.

I would like to thank my parents, Kimiko and Stanley Holloway; brother, Tim Holloway and sister, Shirley Bagshaw for their support and encouragement in each of my activities. Lastly, I would like to thank my friends and the BSO swim team for their very important role of maintaining a stable life in graduate school.

TABLE OF CONTENTS

1. INTRODUCTION

1.1 Porosity

Porous defects in structural materials limit their fatigue and ultimate strength [1,2]. Porous defects in two types of Al-Si-Cu aluminum castings were found to be the initiation fatigue site and to control the fatigue strength and fatigue life [1]. Often, the fatigue crack nucleated at a porous defect and propagated mostly in the eutectic phase [3]. Aluminum castings are known to be difficult to make and contain a number of porous defects [1,4]. Often, a large scatter in the size of porosity exists. This scatter in size appeared to be directly related to the large scatter found in the fatigue life of the aluminum alloys reported in a study by Suzuki and Kunio [1,5,6].

A porous defect is caused by gas evolution and capture during solidification or by shrinkage during solidification [7]. Several papers [4,8,9,10,11] formulated models based on hydrogen partial pressure and the moisture content of the atmosphere when a gas evolution porous defect was created. The shrinkage void was thought to have formed when the interlocking dendrite arms reduce the permeability of the residual melt near the end of the solidification process [4,12]. The pore formed was closely related to the dendrite size. The finer the dendrite size, the smaller the pore formed; and consequently, the reduction in mechanical properties was less [12].

1.2 Scope of This Study

This study was conducted to determine the nature and distribution of porosity in an AlSi 319 alloy used in the automotive industry. Non-destructive testing was investigated as a possible quality-control method for the automotive industry to evaluate the porosity in lost-foam cast aluminum-silicon alloy. Destructive evaluation methods were used to confirm the findings from the non-destructive techniques. The data from the various techniques were correlated to determine the nature and distribution of porosity within the aluminum-silicon alloy.

1.3 Aluminum-Silicon Alloy

Aluminum-silicon alloys have a continuous alpha-aluminum phase with an aluminum-silicon eutectic. The silicon increases the fluidity, strength and hardness (over that of pure aluminum) but decreases the ductility. Copper (up to 12%) adds strength, hardness and improves machinability but lowers the corrosion resistance. Magnesium (up to 6%) helps to increase hardness, strength, corrosion resistance and machinability. Aluminum-magnesium alloys, though, are prone to oxide films and inclusions. Iron is

considered an impurity. Iron and manganese form the intermetallic compound with the appearance of "Chinese Script". Zinc combines with other elements to form intermetallic compounds which help produce strength, toughness and corrosion resistance. Titanium is added (0.1 to 0.25%) to aluminum as a grain refiner [13]. The aluminum-silicon alloy phase diagram is shown in Fig. 1. In general, the solidification occurs in two stages: a framework of elongated dendrites form and is filled with the eutectic melt; then the eutectic crystallizes into cells where the silicon in each cell is interconnected [4,14]. The shape and size of the eutectiferous, silicon crystals can influence the mechanical properties of the alloy. Figure 2 is a photomicrograph of the aluminum-silicon 319 alloy. The silicon crystals, if sharp, may act as internal notches; if smooth as in the modified alloys, the mechanical behavior is generally improved [16]. However, the sharpness versus the smoothness of the silicon eutectic is secondary to more severe stress concentrators such as inclusions and, most importantly in this type of casting, porosity.

1.3.1 Characteristics of the Dendrite

Several papers [3,12,17,18] discussed the relationship of the mechanical properties to features of the dendrite. Grain size measurements were once the preferred structural characteristic used to correlate mechanical properties to various castings. However, the widespread use of grain refiners has decreased its value as a correlator. Presently, values associated with dendrites are being considered to correlate casting conditions to mechanical properties. These values include dendrite cell size, dendrite cell spacing and dendrite arm spacing (DAS). Dendrite cell size is the width of individual cells; dendrite cell spacing is the distance between center lines of adjacent cells; and DAS is the distance between developed secondary arms.

Dendrite cell size and DAS appear to be the best characteristics used for defining relationships. Dendrite cell size is related to the solidification rate and alloy composition. The cell size should decrease with increased alloy addition at a given solidification rate. A smaller cell size generally yields an increase in tensile strength and elongation, but the yield strength will remain constant. The lack of influence upon the yield strength is typical for aluminum alloys [18].

DAS is affected by several solidification variables: solidification time, temperature gradient, cooling rate and freezing index. A finer DAS can be obtained with higher freezing rates or with rapid solidification of the casting. A linear relationship between DAS and the log of each of the variables exists. A finer DAS results in a higher ultimate tensile strength, a slightly higher yield strength and a decrease in percent elongation. A nonlinear relationship exists between the DAS and mechanical properties [17]. For example,

Wickberg et al. [3] found that the fatigue strength of a material was proportional to the (DAS):

$$\text{Fatigue Strength } \alpha \text{ DAS}^{\frac{-1}{2}}$$

The fatigue strength could then be estimated using this equation. The relationship [3] was then extended to estimate the fatigue strength for a given number of cycles (N):

$$\text{Stress Amplitude (N)} = A + B(\text{DAS}^{\frac{-1}{2}})$$

A final note on the application of using dendritic characteristics; the effect (of the dendritic characteristics) upon mechanical properties may be overshadowed by the affects of porosity [18].

Many factors influence the development of structure and properties as a result of casting process [19]. The effects of casting conditions and amount of silicon on volume shrinkage were investigated by Okorofor [14]. Volume shrinkage was associated with the formation of macro-cavities, surface sinks, and internal porosity. Okorofor explained internal porosity on the basis of feeding capacity of the alloy; effective feeding resulted in less internal porosity than a system with inadequate feeding. He investigated pure aluminum through 12% silicon content. Okorofor determined that the amount of internal porosity volume peaked at about 8% and then decreased as the eutectic composition was reached (12% silicon) [14]. This finding suggested that the silicon (up to 8%) hinders the feeding; and thus, the internal porosity increased. Suzuki and Kunio [1] determined that the fatigue life was improved by reducing the size of the porous defect. The elimination of porosity in cast aluminum alloys would be ideal but, unfortunately, not practically obtainable. Therefore, the detection and characterization of the porous defects in these cast alloys is necessary to estimate the performance of the material. Knowledge about the defects and their effect on the mechanical properties will provide designers with a realistic safety margin for design [20]. Non-destructive methods can be effective in characterizing the amount and nature of the porosity (which can then be correlated to mechanical properties.) The ideal characterization method would determine the number of pores and the distribution in size, shape and orientation [2].

1.4 Non-Destructive Testing

Non-destructive testing (NDT) is any type of inspection that does not alter or damage the component under observation but will provide needed information about the part. NDT is often used for quality-control in the manufacturing industry. The type of flaw and its location will dictate the best applicable NDT method [21]. Three NDT methods will be discussed in this paper: radiography, ultrasonics and acoustic microscopy.

1.4.1 Radiography

Radiography is a non-destructive test which is used to detect internal and surface defects. Basically, short wavelength electromagnetic radiation such as x-rays are emitted from a source, pass through the material and are recorded on film. The radiation will be attenuated according to the density and thickness of the material and to the characteristics of the radiation. The differential attenuation of the radiation by different media allows radiography to be an important non-destructive test. For example, the amount of radiation which passes through a defect such as a void or inclusion will be different than that which passes through the base material. This variation will be visible on the film [21,22]. In radiography, defects (or variations) which have a big thickness or density difference between the feature and component, or have an appreciable thickness difference parallel to the radiation beam, or are non-planer produce the best results. Lamination type defects are nearly impossible to detect in radiography [21]. Ref. 23 describes the appearance of defects and discontinuities which can be detected in radiographs.

The radiographic parameters (tube voltage, tube amperage, source size, source to object and object to film distances) also determine the image that is produced. The voltage determines the wavelength. In theory, a very low voltage should result in a high degree of resolution. A degree of unsharpness in the image (seen on the film) results from a non-point source. The region of unsharpness is termed the penumbra and can be reduced by increasing the source to object distance or by decreasing the object to film distance [21,23]. This inherent degree of image unsharpness complicates quantitative studies of certain defects like porosity. However, quantitative information about porosity was obtained by Prasad, Ganesha and Nair [20] who enhanced the radiographs by manually drawing the outlines of the pores and then used an image analysis system to characterize these images.

1.4.2 Ultrasonic Testing

Ultrasonic testing can be used to detect internal and surface flaws. Elastic waves (0.5 MHz to 20 MHz.) can be transmitted through fluids and solids. There exists a limit to the sound transmission between interfaces. For example, sound does not transmit easily

between air and metal. Thus, a coupling agent is needed for sound transmission; or the beam will be totally reflected at the metal/air interface. The beam will also be completely or partially reflected by internal defects such as cracks, delaminations, porosity, and other non-metallic inclusions. The resolution of this method is determined by the wavelength of the sound beam. The wavelength, λ, is directly related to the frequency, f, and the wave velocity, V: $\lambda=V/f$. The objects to be detected must have a size equal to or greater than the wavelength of the particular wave [21].

Another method of material and defect characterization in ultrasonics is the analysis of the attenuation of the beam. Attenuation, loss of energy, occurs continually due to scatter at microscopic interfaces and due to internal friction effects. Sound attenuation is also related to the frequency, density of material, wavelength of ultrasound and various other parameters. The theory is discussed in Refs. 2,21,24. An extensive amount of related work may be found in [25 - 29].

The investigations by Adler, Wang, Csakany, Rose and Mobley [2,30] concluded that pores in aluminum castings could be measured using the attenuation of the ultrasound pulse. Basically, a broad band-width, ultrasonic pulse was produced using a fast rise-time, high voltage, untuned, ceramic transducer. The reflected signals were captured with the same transducer. It was determined that the attenuation of the beam was due to the porosity in the casting and that a weak correlation between the pore size (and attenuation of the beam) was present [2,30].

1.4.3 Acoustic Microscopy

The acoustic microscope visually reveals the interaction between ultrasound and the material being studied. A specimen is studied in the Scanning Laser Acoustic Microscope, SLAM, by pulsing plane, acoustic waves through it. The sound is scattered and absorbed as dictated by the specimen's internal elastic microstructure. A laser beam shines on the specimen surface and detects the displacements which occur as the sound wave propagates. The brightened, mirrored surface is an optical phase replica of the sound wave, and the laser detects the degree of distortion in the periodic wave [31]. Figure 3 is a schematic of the SLAM. The SLAM can be used to study simple and complex shaped parts. The data obtained in the past have been used to investigate the intrinsic elastic properties on the microscopic size basis, characterize grain structure and material texture, evaluate porosity and quantify defects. The SLAM has also been suggested as a tool for studying crack growth as it occurs; the sound will attenuate across the fracture surface (crack region) [32].

There are various ways to produce an image from the distortion of the periodic wave. The most common imaging mode is the transmission mode. The micrograph produced from this method is a shadowgraph of all the structure the sound waves encounter as they pulse through the sample [32]. Inhomogeneities within the specimen will cause variations in the acoustic energy by reflecting or scattering the sound waves. The inhomogeneities which are larger than the acoustic wavelength will be resolved as individual objects on the acoustic micrograph. Those inhomogeneities which are smaller than the wavelength cause scattering to occur. A unique "texture" may result from these small inhomogeneities and may be used to identify specific materials [31]. Attenuation also arises by absorption of the sound by the sample. Phase imaging such as phase contrast imaging and the acoustic interferogram are also widely used imaging modes. The latter mode produces images from the variation in sonic velocity; whereas, the images in the transmission mode were produced from attenuation variations. The image is produced by superimposing a number of constant time of flight fringes called velocity fringes. A velocity fringe will shift to the right if it goes to a higher velocity of sound material and to the left if it goes to a lower velocity of sound material. Therefore an internal or external defect can be imaged by noting the perturbations of the velocity fringes [31]. Various other methods of imaging have been developed such as reflection, acoustic dark field, non-linear acoustic and polarization sensitive acoustic imaging. These methods are versions of the transmission imaging scheme. The image produced by the SLAM can be compared to a radiograph. Several views may be taken to establish the actual three-dimensional shape of the internal features [33].

Roth, Generazio and Baaklini [34] characterized the voids in structural ceramics using the SLAM and found that structural ceramics exhibit wide variability in strength and low fracture toughness because of their brittle nature. Failure was generally attributed to discrete flaws such as microcracks, voids, impurities and oversized grains. The actual diameters of the voids examined were much smaller than the voids predicted using the SLAM. This discrepancy was attributed to the measurement uncertainty and the limitations of 100 MHz SLAM when a typical ceramic specimen was used [34]. Measurement uncertainties arose from analyzing the diffraction patterns where the void was not perpendicular to the direction of sound propagation. In other words, the actual diameter of the void was being compared to a measurement taken from a tilted image of the void which would not produce a true size measurement. Roth et. al. [34] determined that the larger voids situated closer to the surface presented a greater uncertainty in size determination than smaller voids positioned further from the mirrored surface.

The greater accuracy of measuring smaller diameter voids does not imply that the smaller voids are easier to detect. The exact opposite was found in a study by Roth and Baaklini [35]. Larger voids were detected over a greater range of depth than smaller voids. The detection of voids was also diminished in the coarser grained material. The coarser grained material resulted in greater ultrasonic attenuation than the finer grained material which produced a noisier acoustic image. The noisier image was thus more difficult to interpret [35].

It has been shown in numerous papers [32,34,35,36] that the material and void characterization such as size and depth will influence the results of the SLAM experiments. These papers also show that the SLAM can be used as a viable non-destructive evaluation (NDE) technique. Kessler and Oravecz [32] assert that "acoustic microscopes are especially useful since ultrasound penetrates solid materials that are opaque to light, x-ray or infrared. In addition, information is obtained about a sample which relates to its mechanical properties, a most important reason for employing NDT." Presently however, modifications (to the SLAM) are necessary for the SLAM to be a useful quality-control tool in the automotive industry.

1.4.4 Non-Destructive Evaluation Signatures

Combining the information from multiple non-destructive techniques can be used to evaluate the microstructural characteristics of some materials. The various techniques can combine to form a 'non-destructive evaluation signature'. Shannon and Liaw [37] developed a linear superposition model to quantify the influence of microstructural characteristics on the overall non-destructive evaluation signature of several aluminum metal-matrix composites. They correlated ultrasonic velocity, eddy current and resistivity measurements to the presence of silicon-carbide-particulates, intermetallics compounds and porosity. The signatures, however, do not provide information on single defects such as lengths and widths of individual pores.

2. EXPERIMENTAL PROCEDURES

2.1 Material Description and Specimen Geometry

The aluminum silicon alloy (AlSi 319) studied was donated by the General Motors Technical Center. The alloy was cast into bars using the lost-foam method and T5 heat treated. Each of the bars discussed in this report are of similar casting and heat treat populations. The chemical composition of the material was determined by the Chicago Spectro Service Laboratory, Inc. and is shown in Table 1.

The bars were received as cylinders with the dimensions of 15.2 mm (0.6 in.) diameter and 177 mm (7.0 in.) length. Sections for the study of casting porosity were cut from the end of these bars using a diamond cut-off wheel. The sections were 1.3 mm (~0.05 in) thick, 12.7 mm (0.5 in) in diameter. A small hole, 1.3 mm (~0.05 in) diameter, was drilled at the periphery of each section which was used as a locator for each evaluation technique. The sections were polished using a succession of alumina polishing grits down to 0.05 μm. A final polish using Aquafresh ® toothpaste was used to produce a high-quality surface finish.

The bars were machined into standard ASTM fatigue or tensile specimens. The tensile and fatigue tests were were conducted as a separate part of the project with the General Motors Technical Center [38]. The hardness and monotonic properties of the alloy are shown in Table 2.

2.2 Observation of Casting Porosity Using Radiography

Radiography was used to study the three-dimensional nature of the casting porosity. The polished sections were placed directly on DuPont NDT Daypack 35 film with the polished face toward the X-ray source. DuPont NDT 35 Daypack film is a high resolution ASTM Class I film (low graininess, high contrast). The radiographic parameters chosen for the Andrex Portable Set were 95 kV tube voltage, 5 mA tube current, a X-ray source to specimen distance of 1245 mm (49 in.), and an exposure time of 2 minutes. These parameters were chosen not for optimum radiographic images but for the optimum quality of the photographic prints produced using the radiograph as a negative.

Enlarged photographic prints, by B & W Corley Photographers of Champaign, IL, were produced on high-contrast, contact paper directly from the radiographs. The photographic prints obtained were the negative of the actual image (i.e., the pores were white instead of black on the photographs). Figure 4 is an enlarged photographic print of the polished section 49 End radiograph.

2.3 Observation of Casting Porosity Using the Scanning Electron Microscope

A scanning electron microscope (SEM) was used to study the casting porosity in the polished sections and the pores initiating fatigue failure in the fatigued specimens. The SEM actually images an excited volume of material near the surface and not the surface of the sample, per se. A large excited volume occurs in aluminum due to its low atomic number. To enhance the image quality and increase the resolution of surface detail, a thin layer of gold was sputtered onto both the polished sections and fatigue fracture surfaces prior to observation in the SEM. The polished surfaces of the sections and the fracture surfaces were sputtered with gold using an EMScope SC 400 coater for 1.5 minutes at 20 mA. This coating was also required for subsequent studies using the acoustic microscope, discussed below.

Low magnification (30X) montages of SEM photographs were prepared for the polished sections. Figure 5 is a montage of polished section 49 End. Higher magnification photographs of individual pores were also taken, and the length (L) and width (W) were measured from these high magnification photographs. The definition of these dimensions may be seen in Fig. 6. Figures 7 and 8 are photographs of pores A and B (labelled in Fig. 5) at 100 X.

Fracture surfaces of failed, uniaxial fatigue loaded specimens were obtained from the separate project with the General Motors Technical Center [38]. Each pore initiating fatigue failure was photographed using the SEM. The length (2C) and width (a) of each pore initiating fatigue failure were measured from the prints. The definition of the dimensions (2C and a) may be seen in Fig. 6. Figure 9 is a SEM photograph of a pore initiating fatigue failure at 78 X in fatigue sample 3.

2.4 Observation of Casting Porosity Using the Optical Microscope

Although the SEM is by far the superior method for observing casting porosity, several polished sections were studied using a reflected light optical microscope (OM). The dimensions of pores were more easily obtainable using the OM. The OM had a measuring eyepiece by which the length (L) and width (W) were measured for each visible pore on the polished section. Figures 11 and 12 are OM images of individual pores. The definition of the dimensions may be seen in Fig. 6.

2.5 Observation of Casting Porosity Using the Acoustic Microscope

A SonoScan Scanning Laser Acoustic Microscope (SLAM) at 100 MHz in the Bioacoustic Laboratory at the University of Illinois at Urbana-Champaign was used to obtain optical and acoustic images of the internal and surface porosity within a polished

section. If necessary, the polished sections were re-coated with gold for analysis using the SLAM to provide a reflective coating, as discussed in Section 1.4.3. Optical and acoustic observations were recorded using 35 mm film. Optimum settings for obtaining the acoustic images were determined for each polished section examined. The reader is referred to Ref. 39 for obtaining optimum settings since each polished section required different adjustments. Figure 12 is a montage of the acoustic image of the entire polished section 49 End. Figures 13 and 14 are acoustic images of individual pores (labelled A and B in Fig. 5).

2.6 Determination of Areal Fraction of Casting Porosity

Porosity areal fractions were determined using the enlarged optical photographs of polished sections. A transparency of polar coordinate graph paper was overlaid on the enlarged photograph and used as a grid to count the intersection of pores with the grid. The number of porosity indication intersections divided by the number of overall possible intersections determines the areal fraction of porosity. See Ref. 40 for a discussion of this technique.

3. RESULTS

3.1 Observations of the Casting Porosity Using Radiography

The polished sections appear as circular, gray images on the photographic print of the radiograph as seen in Fig. 4. The white circle at the 12 o'clock periphery position within the gray image is the locator hole which was drilled into the sample. Faint, indistinct, white regions and narrower, more distinct, white regions are apparent on the print. Photographic prints for the individual white regions could not be produced due to the indistinctness of the radiographs. Damage to this polished section occurred while polishing and appears as faint white regions in the shape of three half-circles The damage is located in the 3 o'clock position on the radiographic print.

3.2 Observations of the Casting Porosity Using Scanning Electron Microscopy

The montage of the 30X, SEM photographs is roughly spherical. The locator hole is filled with a graphite adhesive. The adhesive was necessary to attach the polished section to the SEM specimen holder. The damage that occurred to this specimen is located at the edge of the montage in the 2 o'clock position just above the lighter gray patches of (30X SEM) prints and appears as white, highlighted areas. No smearing of the edge of the pores due to polishing was evident at higher magnifications. The appearance of two pores, A and B (labelled in Fig. 5), is shown in Figs. 7 and 8. The orientation of pore A of the SEM photograph with respect to the optical photograph is marked with an arrow and the letter, N.

SEM photographs of the pores initiating fatigue failure were taken. Figure 9 is a SEM photograph of a pore initiating fatigue failure in fatigue sample 3. This pore is a shrinkage pore and was modelled as a semi-elliptical pore at the surface. The dimensions taken from the pores initiating fatigue failure were 2C and a: see Fig. 6 A. The data for the pores initiating fatigue failure are listed in Table 3. Complete information regarding the (fatigue) history of the fatigue loaded samples may be found in Ref. 38.

3.3 Observations of the Casting Porosity Using Optical Microscopy

Figures 10 and 11 show the appearance of pores A and B in the OM. The silicon eutectic is probably apparent due to polish relief and the natural color of the eutectic. The specimen was not etched. The same type of measurements were taken using the OM as those taken using the SEM on the polished sections. The lengths and widths of the pores measured using the OM were combined with the data obtained using the SEM. The lengths

and widths of the pores are recorded in Tables 4 - 8. The number of pores in the classes 'a' and W and 2C and L are in Tables 9 and 10.

The General Motors Technical Center provided data in the form of equivalent diameters of pores in Bar 7 through the use of an image analyzer: see Table 11. The true dimensions of the pores; length, L, and width, W, observed on the sections of Bar 7 were not reported. Two sections were cut from Bar 7: one section was cut from a dark area and one section was cut from a light area as observed on the radiograph of Bar 7.

3.4 Observations of the Casting Porosity Using Acoustic Microscopy

The acoustic image using the SLAM has a mottled black and white background with large dark patches. Pores appear as solid, black patches. A montage of prints was assembled for polished section 49 End: see Fig. 12. The index hole appears in the 12 o'clock periphery position. The damage that occurred to this sample during polishing is located in the 3 o'clock position and appears as two hemispherical, black regions. The distinct, narrow white rectangle at the 10 o'clock position is an artifact introduced during the photographic reproduction of the montage. Figures 13 and 14 are photographs of acoustic images of pores A and B (labelled in fig. 5).

3.5 Determination of Areal Fraction of Casting Porosity

The areal fractions of porosity determined by quantitative metallography of the polished sections of the polished sections are listed in Table 12.

4. DISCUSSION

4.1 Comparison of the Several Techniques Used to Observe Casting Porosity

All observational methods used in this study proved capable of detecting casting porosity. The porosity indications for each method were compared to those of other methods to verify that the indications were in fact porosity. A comparison of the results obtained using the several techniques used is available in Figs. 8, 9, 11, 12, 14 and 15 in which the pores A and B (labelled in Fig. 5) were examined at medium magnification using SEM (100X), optical (78X) and SLAM (30X).

The SEM and OM methods show the porosity clearly on the plane of polish. However, having only the plane of polish available for observation could pose a problem as is illustrated in Fig. 7 which shows a SEM micrograph of a pore just intercepting the plane of polish. The largest dimension of the pores appearing on the plane of polish is not readily apparent since it may be below (or above) the plane of polish. Even though the SEM and OM produce the best quality images of pores, complete information regarding their size and shape can not be conclusively obtained from these methods.

Surface pores observed on the SEM and OM prints correlated with observations of fuzzy white regions on the radiographic prints. For example, two pores, A and B, of the polished section 49 End are marked on the enlarged, radiographic print (Fig. 4) and SEM montage (Fig. 5). Some of the white regions on the radiographic print did not match the location of any pore observed on the optical photograph or SEM montage and are attributed to pores included in the volume of the polished section but not appearing on its polished surface. Radiography and acoustic microscopy are two non-destructive techniques which give an outline image of the entire pore. Radiography is presently used as a non-destructive evaluation technique in the automotive industry for quality control purposes. The SLAM, if it can be adapted to analyze thicker specimens, will be a powerful non-destructive evaluation tool for quality control in the automotive industry.

Questions were raised during the SLAM investigation as to the identification of the dark patches seen in Fig. 12: were these observations due to porosity or to the silicon eutectic? The SLAM is capable of producing its own reflected laser light surface images separate from the surface and internal acoustic images. The pores at the plane of polish seen in the acoustic image were positively identified as pores by comparing them to the reflected light images taken in the same location. Therefore, the large dark patches were identified as pores. The large dark patches not correlating to a surface pore were assumed to be images of internal pores. The mottled black and white background is believed to be caused by scattering by the aluminum-silicon eutectic phase: see Fig. 2.

4.2 Pore Geometry

The general shape of the pores was determined from the radiographic and acoustic image prints. The radiographic images of the pores were either faint and round or bright, long and narrow: see Fig. 4. These two types of outline images suggest that the pores are irregular discs which may have any spatial orientation. These observations were confirmed using the acoustic microscope.

4.2.1 Pore Size

The information gathered from polished sections can lead to erroneous conclusions about the actual size and shape of pores. The plane of polish may reveal what appears to be small, closely, scattered pores when, in actuality, the scattered pores are the exposed segments of a larger, single pore. Figure 7 is a SEM micrograph of pore A (identified in Fig. 5) in which the center section "caved in", outlining the larger, single pore. If the center section had not collapsed, the SEM or OM image of the pore would not have revealed whether this pore was a single entity or several, smaller pores. An image of a single pore rather than several, smaller pores is revealed in the SLAM acoustic image of this same area: see Fig. 13.

Early in the study the eutectic cell size was thought to govern the pore size. The appearance of the aluminum - silicon eutectic is in Fig. 2. The relationship between the aluminum - silicon eutectic and pore is shown in Figs. 10 and 11. There does not appear to be an obvious correlation between the eutectic cell size and the pore size.

4.2.2 Porosity Percentage

Areal fractions of porosity were measured from the optical photographs of the polished sections using the point count method [40] and are reported in Table 12. Large differences in the percentage of porosity were observed between the supplied bars. Bar 49 had the greatest amount of porosity (≈2.40%) and Bar 6 had the least amount of porosity (0.03%). The average porosity was 0.62%. These porosity percentages were usually determined from only one section of the bar.

A variation in the amount of porosity from end to end of the bar was evident when two sections were analyzed from the same bar. (The casting direction was unavailable.) However, the percentages in question and the sample population are small; and thus, the variations may be within the statistical deviation of a larger population.

4.3 Distribution of Pore Sizes

The dimensions of the pores initiating fatigue failure and the pores from the polished sections were plotted in the histograms shown in Figs. 15 and 16. The average dimension (a) of the pores initiating fatigue failure (Fig. 15) is 0.4 mm with a lower bound of 0.2 mm and an upper bound of 0.7 mm. The average dimension (2C) of the pores initiating fatigue failure (Fig. 16) is 0.6 mm with a lower bound of 0.1 mm and an upper bound of 1.8 mm. There is no distinct distribution evident in the histogram of (a) of the pores initiating fatigue failure. The histogram of 2C of the pores initiating fatigue failure appears to have a lognormal distribution. The size of the pores initiating fatigue failure indicates that the largest pores are those initiating fatigue failure. Previous studies conducted on this material [38,41] also report that the largest pore initiates fatigue failure. No obvious upper bound of pore size is suggested by the histograms (Figs. 15 and 16).

The lengths and widths of the pores observed on the polished sections using optical methods were also plotted. In making these direct measurements, the general outline of the entire pore and whether an associated smaller pores should be included as a part of the larger pore's overall size was decided on a case-by-case basis. The results of these measurements are listed in Tables 3 - 10. The average width (W) of the pores from the polished sections is 0.2 mm with a lower bound of 0.03 mm and an upper bound of 0.6 mm: see Fig. 17. The average length (L) of the pores from the polished sections is 0.3 mm with a lower bound of 0.02 and an upper bound of 1.3 mm: see Fig. 18. The distributions for the width (W) and length (L) of the pores measured on polished sections has a nearly lognormal distribution [42]. The distribution for the length is spread over a greater range than is the distribution for the width. It is unclear whether small pores exist, but they were not visible at the magnifications used in the optical method. Thus, the curve may actually be exponential in nature.

The lengths and widths of the pores observed on the polished sections were not correlated to the 2C and 'a' of the pores initiating fatigue failure. The pores on the polished sections could be in any spatial arrangement as discussed in Section 4.2; and thus, a correlation between the two types of dimensions would not be accurate. However, the pores initiating fatigue failure were generally within the limits of the large pores observed on the polished sections. One pore initiating fatigue failure (2C) was larger than any pore seen on the polished sections.

The General Motors Technical Center data for Bar 7 were plotted as a histogram, and the distribution of pore sizes was roughly an exponential function. The average is 0.6 mm with no pore exceeding 0.23 mm in diameter, see Fig. 20. The image analyzer results

(Table 11) from the General Motors Technical Center have a higher frequency of small pores than the data of pore sizes from the SEM/OM, pores initiating fatigue failure, or radiography: see Figs. 15 - 20. An overestimate of the number of small pores by the image analyzer seems to have occurred. However, the results from the General Motors Technical Center are representing two sections of the same bar and not a compilation of many bars. Thus, the results are only a preliminary indication of what an image analyzer is capable of accomplishing and should by no means dissuade the further development of the image analyzer to its full potential in the area of defect size characterization.

Access to an image analyzer at the University of Illinois-Urbana was limited; and thus, only hypotheses can be made as to the overestimate of the number of small pores by the image analyzer. The first hypothesis is that the equivalent circle diameter given by the image analyzer is smaller than the true dimensions (length and width) of a pore. Thus, a high frequency of small pores is reported. Secondly, the image analyzer distinguishes objects by gray levels; therefore, the pore seen in Fig. 7 will not have a constant level of gray throughout the large pore area. The pore may thus be identified (by the image analyzer) with a different gray level associated with each segment of the pore (the segments are discussed in Section 4.2.1). Each coherent gray level would be identified as a separate identity. Therefore, the large, single pore would be reported as several small pores resulting in an unusually high frequency of small pores.

The largest dimension measured from the enlarged prints of the radiographs of the polished sections has an average of 0.4 mm with a lower bound of 0.1 mm and an upper bound of 1.7 mm. The average from the enlarged, radiographic prints is close to the average of the pores initiating fatigue failure ($2C = 0.6$ mm and $a = 0.4$ mm). Small pores were not obvious on the enlarged photographic print of the radiographs. The distinctness of any feature on the radiograph was lost when it was enlarged and printed on contact paper. (An adjustment for the penumbra effect was not included in the measurements.) Thus, the smaller pore sizes were not included in the average of 0.4 mm; consequently, the average is larger than for the average obtained using the SEM or OM. The general nature of the distribution for the radiography method is similar to that obtained for the pores initiating fatigue (2C), and for the pores (L and W) measured using the SEM or OM on the polished sections: see Figs. 16, 17, 18 and 19.

No method could prove or disprove an existence of a limit to the smallest size of a pore.

4.4 Suggestions for Future Work

The experience gained in this study suggests several improvements in technique which should be included in future work:

a. Consider determining the pore size distribution using a radiograph image manually edited and then measured using an image analyzer.

b. Invest the resources in duplicating for AlSi 319 lost-foam cast alloy the ultrasound experiments of Ref. 7 discussed in Section 1.4.2 .

c. Develop techniques for the non-destructive testing of thick samples using the SLAM.

d. Determine non-destructive evaluation signatures for AlSi 319 lost-foam cast alloy as discussed in Ref. 37.

e. Develop a relationship between percent porosity and the possible size of the largest pore.

f. Investigate further the spatial distribution of porosity within the individual cast samples.

5. SUMMARY AND CONCLUSIONS

Three goals were the motivation for this investigation: First, study the nature of the porosity in lost-foam cast AlSi 319 alloy; second, determine the distribution of porosity which is essential in developing the stochastic modelling of the fatigue life of this alloy; third, use non-destructive techniques which may be adapted for quality control in the automotive industry. The performance of the non-destructive techniques were evaluated by comparing the non-destructive results to destructive evaluation results.

The conclusions drawn from this investigation are summarized as follows.

1. The pores are shaped as irregular disks without spatial orientation.
2. The (2C), (L), (W) and measurements from the radiographic prints had similar lognormal distributions.
3. The distribution of the critical dimension (a) of the pores initiating fatigue failure did not follow a recognizable function.
4. Each of the techniques used in this study was capable of detecting porosity. Although, the scanning laser acoustic microscope (SLAM) has not been widely used in the study of metals, it is expected to become a powerful non-destructive tool in the evaluation of metals and other materials.

6. REFERENCES

1. Suzuki, H., Kunio, T.; "Influences of Porous Defect on Scatter of Fatigue Strength of Aluminum Casting Alloy, AC4B (JIS)", Proceedings from: Role of Fracture Mechanics in Modern Technology, Edited by Sih, G.C., Nisitani, H., Ishihara, T.; Elsevier Science Publishers B.V., North-Holland (1987), p. 225.

2. Adler, L., Rose, J. H., Mobley, C.; "Ultrasonic Method to Determine Gas Porosity in Aluminum Alloy Castings Theory and Experiment", Journal of Applied Physics, Volume 59, No. 2, (1986), p. 336.

3. Wickberg, A., Gustafsson, G., Larsson, L.E.; "Microstructural Effects on the Fatigue Properties of a Cast A17SiMg Alloy", Society of Automotive Engineers, Inc., Deerfield, IL, (1984), p. 1.

4. Dunkel, E.; "On the Formation of Porosity in Aluminium and Aluminium-Silicon Alloys", Giessereiforschung in English, Volume 22, No. 4, (1970), p. 178.

5. Suzuki, H. et. al.; "Rolls of Microstructure and Mechanical Properties on Fatigue Strength of Vermicular and Nodular Iron", Transactions of JSEM, 50-451, A (1984), p. 520.

6. Suzuki, H. et al.; "Influence of Matrix Structure on Fatigue Strength of Nodular Iron with High Tensile Strength", Transactions of JSME, 51-464, A (1985), p. 1225.

7. Piwonka, T.S., Flemins, M.C.; "Pore Formation in Solidification", Transactions of the Metallurgical Society, AIME, Volume 236, (1966), p. 336.

8. Yeum, K., Poirier, D.R.; "Predicting Microporosity in Aluminum Alloys", Proceedings from: Light Metals 1988 Phoenix, AZ.; The Metallurgical Society, Inc., Warrendale Pennsylvania, (1988), p. 469.

9. Kubo, K., Pehlke, R.D.; "Mathematical Modeling of Porosity Formation in Solidification", Metallurgical Transactions B, Volume 16B, (1985), p. 359.

10. Closset, B., Gruzleski; "Modification, Porosity and Hydrogen Content in Al-Si Casting Alloys", Proceedings from: 56th World Foundry Congress; Technical Communication, USA, (1989), p. 32.

11. Argo, D., Gruzleski, J.E.; "Porosity in Modified Aluminum Alloy Castings", Transactions American Foundrymens Society, Volume 96, No. 16, (1988), p. 65.

12. Rostoker, W., Dvorak, J.R.; Interpretation of Metallographic Structures, Second Edition. Academic Press, New York, New York, (1977), p. 114.

13. Wabash Alloys Division, "Metallurgy of Aluminum Casting Alloys", Aluminum Alloys Handbook, Wabash Indiana, (1976), p. 16.

14. Okorafor, O.E.; "Some Considerations of the Volume Shrinkage of Aluminium-Silicon Alloy Castings Produced in Full Moulds", Transactions of the Japan Institute of Metals, Volume 27, No. 6, (1986), p. 463.

15. Corson, M.G.; Aluminum the Metal and Its Alloys. D. Van Nostrand Company, New York, New York, (1926), p. 72.

16. Brick, Gorden, Phillips; Structure and Properties of Alloys. McGraw-Hill Book Company; New York, New York, (1965), p. 165.

17. Radhakrishna, K., Seshan, S., Seshadri, M.R.; "Dendrite Arm Spacing in Aluminum Alloy Castings", Transactions American Foundrymens Society, Volume 80, (1987), p. 695.

18. Spear, R.E., Gardner, G.R.; "Dendrite Cell Size", Modern Castings, Volume 43, No. 5, (1963), pp. 209-215.

19. Okorafor, O.E., Lopre Jr., C.R., "Modification and Properties of Expendable Polystyrene Pattern Cast Al-6.5Si-3.5Cu", The Foundryman, (1988), p. 136.

20. Prasad, J., Ganesha, H.S., Krishnadas Nair, C.G.; "Quantitative Radiography and Defect-Property Correlation in Aeronautical Castings", Proceedings from: Through The Eyes Of an Eagle, 11th World Conference on Nondestructive Testing, Edited by Jones, L.K., et al.; Taylor Publishing Co., Dallas, Texas, (1985), p. 505.

21. Hull, B., John, V.; Non-Destructive Testing. Springer-Verlag New York Inc., New York, New York, (1988).

22. Instruction Manual, Instructions for Use of ANDREX Portable X-Ray Equipment. Picker Andrex X-Ray A/S. A Picker Corporation Subsidiary, Copenhagen S. Denmark.

23. Standard Reference Radiographs for Inspection of Aluminum and Magnesium Castings, ASTM Designation: E 155-85, (1985).

24. Papadakis, E.P.; "Ultrasonic Attenuation Caused by Rayleigh Scattering by Graphite Nodules in Nodular Cast Iron", Journal of Acoustical Society of America, Volume 70, No. 3, (1981), p. 782.

25. Gubernatis, J.E. and Domany, E., Proceedings from: In Review of Progress in Quantitative Nondestructive Evaluation; Edited by Thompson, D.O., Chimenti, D.E.; Plenum, New York, Volume 2A, (1983), p. 833.

26. Evans, A.G., Tittmann, B.R., Ahlberg, L., Khuri-Yakub, B.T., Kino, G.S.; Journal of Applied Physics, Volume 49, (1978), p. 2669.

27. Varadan, V.K., Ma, Y., Varadan, V.V.; Journal of Acoustical Society of America, Volume 77, (1985), p.375.

28. Thompson, D.O., Wromley, S.J., Rose, J.H., Thompson R.B.; Proceedings from: In Review of Progress in Quantitative Nondestructive Evaluation; Edited by Thompson, D.O., Chimenti, D.E.; Plenum, New York, Volume 2A, (1983), p. 867.

29. Varadan, V.K., Varadan, V.V., Adler, L.; Proceedings from: Nondestructive Methods in Materials Evaluation; Edited by Ruud, C.O., Green, R.E.; Plenum, New York, New York, (1984), p. 179.

30. Wang, S.W., Mobley, C.; "Ultrasonic Determination of Porosity", Proceedings from: Review of Progress in Quantitative Non-Destructive Evaluation; Plenum Press, New York, (1985); Volume 4B, p. 919.

31. Kessler, L., Yuhas, D.E.; "Acoustic Microscopy 1979", Proceedings from: IEEE Volume 67, No. 4, (1979), p. 526.

32. Kessler, L., Oravecz, M.G.; "Scanning Laser Acoustic Microscope (SLAM) Analysis of Advanced Materials fro Internal Defects and Discontinuities", Sonoscan Inc.: 530 E. Green St. Bensenville, IL 60108.

33. Lin, Z.C., Wade, G., Lee, H., Oravecz, M.G.; "Subsurface Imaging in Acoustic Microscopy", Proceedings from: Acoustical Imaging; Volume 15, Plenum, New York, (1987), p. 443.

34. Roth, D.J., Generazio, E.R., Baaklini, G.Y.; "Quantitative Void Characterization in Structural Ceramics by Use of Scanning Laser Acoustic Microscopy, Materials Evaluation, Volume 45, (1987), p. 958.

35. Roth, D.J., Baaklini, G.Y.; "Reliability of Scanning Laser Acoustic Microscopy for Detecting Internal Voids in Structural Ceramics", Advanced Ceramics Materials, Volume 1, No. 3, (1986), p. 252.

36. Kupperman, D.S., Lee, P., Yuhas, D., McGraw, T.E.; "Acoustic Microscopy Techniques for Structural Ceramics", Ceramic Bulletin, Volume 59, No. 8, (1979), p. 814.

37. Shannon, R.E. and Liaw, P.K.; "Correlation of Microstructural Characterization with Nondestructive Evaluation of Al/SiC Metal-Matrix Composites", to be submitted to Metallurgical Transactions A, (1989).

38. Biell, A.J.; "The Effect of Casting Porosity on the Fatigue Life of Lost-Foam Cast Iron and Aluminum-Silicon 319". Master's Thesis, Metallurgical Engineering, University of Illinois-Urbana. (1989).

39. Operations manual for the SonoScan Scanning Laser Acoustic Microscope, Sonoscan Inc.: 530 E. Green St. Bensenville, IL 60108.

40. Underwood, E. E.; "Quantitative Metallography", Metals Handbook Volume 1, 8th Edition. American Society for Metals, Metals Park, Novelty, OH, (1961), p. 123.

41. Siljander, A., Lawrence Jr., F.V.; "The Mechanical Properties of Al-Si 319, The Role of Casting Porosity". Report to the General Motors Corporation, College of Engineering, University of Illinois at Urbana-Champaign, Urbana, IL, (1988).

42. Ting, J., Lawrence, F.V.; "The Long Life Fatigue Strength Prediction of Lost-Foam Cast 319 Al-Si Alloy, A Probability-Based Model". Unpublished report to the General Motors Corporation, College of Engineering, University of Illinois at Urbana-Champaign, Urbana, IL, (1989).

7. TABLES

TABLE 1

CHEMICAL COMPOSITION OF ALUMINUM-SILICON 319 ALLOY IN WEIGHT PERCENT*

Si	Cu	Mg	Fe	Ti	Zn	Mn	Pb	Sn	Ni	Cr
5.50	3.51	0.35	0.32	0.11	0.76	0.19	<0.05	<0.05	<0.05	<0.05

* Chicago Spectro Service laboratory, Inc., 4848 S. Kedzie Ave., Chicago, IL 60632 provided this chemistry evaluation.

TABLE 2

MONOTONIC PROPERTIES OF LOST-FOAM CAST ALUMINUM SILICON 319 ALLOY IN LABORATORY AIR

Ultimate Tensile Strength (MPa)	228.1
0.2% - Offset Yield Strength (MPa)	228.1
Percent Reduction in Area (%)	0.26
Brinell Hardness (BHN) †	52.0

† 10 mm ball with a 500 Kg load

TABLE 3

FATIGUE FAILURE INITIATION SITE DIMENSIONS †

SAMPLE IDENTIFICATION	2C (mm)	a (mm)
2	0.71	0.50
3	0.20	0.20
4	0.57	0.47
8	0.45	0.30
11	*	*
12	0.36	0.31
13	0.37	0.59
14	*	*
15	0.40	0.23
16	*	*
20	0.80	0.40
21	*	*
30	0.49	0.48
34	0.10	0.21
35	1.83	0.53
50	1.14	0.74
51	0.71	0.47
56	0.36	0.71
65	0.29	0.30
Average.	0.58	0.43
Std. Dev	0.43	0.17

† See Fig. 6 for definition of dimensions
* Sample was fatigue tested but data was unavailable

TABLE 4

OPTICAL MEASUREMENTS OF PORE SIZE DIMENSIONS FROM SAMPLE 2 †

	L (mm)	W (mm)	W/2 (mm)
	0.15	0.14	0.07
	0.14	0.10	0.05
	0.12	0.06	0.03
	0.16	0.08	0.04
	0.21	0.08	0.04
	0.12	0.05	0.03
	0.22	0.10	0.05
	0.17	0.06	0.03
	0.05	0.05	0.03
	0.06	0.03	0.02
	0.06	0.05	0.03
	0.16	0.08	0.04
Average	0.14	0.07	0.04
Std. Dev.	0.06	0.03	0.01

† See Fig. 6 for definition of dimensions

TABLE 5

SAMPLE 2 END

OPTICAL MEASUREMENTS OF PORE SIZE DIMENSIONS FROM SAMPLE 2 END

L (mm)	W (mm)	W/2 (mm)		L (mm)	W (mm)	W/2 (mm)
0.29	0.16	0.08		0.68	0.48	0.24
0.40	0.16	0.08		0.11	0.05	0.03
0.73	0.41	0.20		0.24	0.17	0.08
0.26	0.16	0.08		0.20	0.15	0.07
0.14	0.08	0.04		0.32	0.21	0.10
0.14	0.19	0.09		0.38	0.15	0.07
0.18	0.17	0.08		0.29	0.19	0.09
0.18	0.15	0.07		0.09	0.05	0.03
0.29	0.26	0.13		0.06	0.06	0.03
0.14	0.10	0.05		0.36	0.34	0.17
0.13	0.08	0.04		0.09	0.05	0.03
0.08	0.03	0.01		0.09	0.05	0.03
0.16	0.10	0.05		0.09	0.05	0.03
0.05	0.05	0.03		0.26	0.21	0.10
0.05	0.05	0.03		0.75	0.31	0.16
0.29	0.18	0.09		0.38	0.21	0.10
0.18	0.10	0.05		0.42	0.20	0.10
0.16	0.13	0.06		0.10	0.06	0.03
0.25	0.15	0.07		0.35	0.35	0.18
0.10	0.10	0.05		0.10	0.08	0.04
0.31	0.18	0.09		0.05	0.05	0.03
0.29	0.21	0.10		0.05	0.05	0.03
0.18	0.16	0.06		0.08	0.08	0.04
0.16	0.14	0.07		0.10	0.10	0.05
0.13	0.08	0.04		0.42	0.17	0.08
0.15	0.10	0.05		0.43	0.29	0.15
0.21	0.10	0.05		0.32	0.32	0.16
0.18	0.12	0.06		0.21	0.15	0.07
0.24	0.24	0.12		0.25	0.20	0.10
0.08	0.05	0.03		0.25	0.11	0.06
0.21	0.05	0.03		0.62	0.29	0.15
0.48	0.25	0.13		0.20	0.16	0.08
0.20	0.16	0.08		0.36	0.15	0.07
0.38	0.34	0.17		0.23	0.19	0.09
0.20	0.08	0.04		0.39	0.31	0.16
0.10	0.05	0.03		0.05	0.05	0.03
0.33	0.29	0.14		0.15	0.15	0.07
			Average	0.24	0.16	0.08
			Std. Dev.	0.16	0.10	0.05

TABLE 6

OPTICAL MEASUREMENTS OF PORE SIZE DIMENSIONS FROM MIDDLE OF SAMPLE 49

	L (mm)	W (mm)	W/2 (mm)
	0.50	0.31	0.16
	1.04	0.26	0.13
	0.17	0.26	0.13
	0.40	0.08	0.04
	0.39	0.16	0.08
	0.94	0.21	0.10
	0.51	0.19	0.09
	0.51	0.38	0.19
	1.30	0.41	0.21
	0.52	0.29	0.15
	0.29	0.19	0.10
	0.15	0.08	0.04
	0.31	0.08	0.05
	0.31	0.30	0.15
	0.38	0.21	0.10
	0.48	0.38	0.19
	0.27	0.21	0.10
	0.32	0.16	0.08
	0.31	0.21	0.10
	0.42	0.05	0.03
	0.63	0.31	0.16
	0.54	0.33	0.16
	0.31	0.29	0.15
	0.10	0.08	0.04
	0.05	0.05	0.03
	0.10	0.05	0.03
	0.47	0.08	0.04
	0.30	0.30	0.15
	0.47	0.21	0.10
	0.44	0.21	0.10
	0.37	0.29	0.14
	0.52	0.22	0.11
	0.32	0.29	0.14
	0.16	0.10	0.05
	0.10	0.08	0.04
	0.42	0.06	0.03
	0.20	0.15	0.07
	0.15	0.04	0.02
Average	0.40	0.20	0.10
Std. Dev.	0.26	0.11	0.05

TABLE 7

OPTICAL MEASUREMENTS OF PORE SIZE DIMENSIONS FROM 0.05 INCHES FROM THE END OF SAMPLE 49 †

	L (mm)	W (mm)	W/2 (mm)
	0.60	0.38	0.19
	1.04	0.11	0.06
	0.34	0.26	0.13
	0.03	0.03	0.01
	0.36	0.11	0.06
	0.03	0.03	0.01
	0.05	0.03	0.01
	0.03	0.01	0.01
	0.03	0.03	0.02
	0.01	0.01	0.01
	0.02	0.02	0.01
	0.02	0.01	0.01
	0.02	0.01	0.01
	0.14	0.09	0.04
	0.10	0.07	0.04
	0.17	0.16	0.08
	0.11	0.09	0.02
	0.23	0.07	0.03
	0.55	0.11	0.06
	0.14	0.08	0.04
	0.11	0.09	0.05
	0.20	0.16	0.08
	0.56	0.42	0.21
	0.19	0.19	0.09
	0.10	0.08	0.04
	0.11	0.10	0.05
	0.34	0.19	0.09
	0.21	0.19	0.09
	0.37	0.34	0.17
	0.26	0.18	0.09
	0.37	0.16	0.08
	0.14	0.14	0.07
	0.37	0.33	0.17
	0.24	0.08	0.04
	0.18	0.14	0.07
	0.37	0.15	0.07
Average	0.23	0.13	0.06
Std. Dev.	0.21	0.11	0.05

† See Fig. 6 for definition of dimensions

TABLE 8

OPTICAL MEASUREMENTS OF PORE SIZE DIMENSIONS FROM END OF SAMPLE 49

PORE IDENTIFICATION †	L (mm)	W (mm)	W/2 (mm)
A	0.73	0.42	0.21
B	0.33	0.30	0.15
C	0.53	0.43	0.22
D	0.09	0.03	0.02
D*	0.26	0.03	0.02
E	0.19	0.18	0.09
F	0.48	0.17	0.08
G	0.75	0.29	0.14
H	0.37	0.13	0.06
I	0.40	0.21	0.10
I '	0.07	0.05	0.02
I '*	0.28	0.18	0.09
J	0.55	0.55	0.28
K	0.38	0.24	0.12
L	0.35	0.25	0.12
M	0.17	0.09	0.04
N	1.13	0.45	0.22
O	0.31	0.09	0.04
P	0.19	0.14	0.07
Q	0.81	0.21	0.10
R	0.08	0.04	0.02
S	0.28	0.11	0.06
T	0.41	0.25	0.12
U	0.73	0.35	0.18
V	0.46	0.26	0.13
W	0.24	0.13	0.06
X	0.16	0.11	0.06
Y	0.14	0.04	0.02
Z	0.29	0.09	0.04
AA	0.70	0.14	0.07
BB	0.88	0.27	0.14
CC	0.44	0.29	0.14
DD	0.57	0.48	0.24
EE	0.48	0.17	0.08
FF	0.26	0.12	0.06
Average	0.41	0.21	0.10
Std. Dev.	0.25	0.14	0.07

† The pore positions may be seen on the SEM montage (figure 5).

* Collective dimensions of closely scattered porosity.

TABLE 9

NUMBER OF PORES
DIMENSIONS: a, W

INTERVAL (mm)	FRACTURE SURFACE OBSERVATIONS	POLISHED DISK OBSERVATIONS				
		2*	2	49*	49†	49m
0.00 - 0.05	0	1	1	4	8	1
0.05 - 0.10	0	21	8	4	8	10
0.10 - 0.15	0	12	3	7	6	1
0.15 - 0.20	0	20	0	4	8	5
0.20 - 0.25	3	7	0	3	0	7
0.25 - 0.30	0	5	0	6	1	6
0.35 - 0.40	3	5	0	1	2	5
0.45 - 0.50	0	1	0	1	1	2
0.50 - 0.55	1	1	0	2	1	1
0.55 - 0.60	3	1	0	2	0	0
0.60 - 0.65	2	0	0	0	0	0
0.65 - 0.70	1	0	0	1	0	0
0.70 - 0.75	0	0	0	0	0	0
0.75 - 0.80	0	0	0	0	0	0
0.80 - 0.85	2	0	0	0	0	0
0.85 - 0.90	0	0	0	0	0	0
0.90 - 0.95	0	0	0	0	0	0
0.95 - 1.00	0	0	0	0	0	0
1.00 - 1.05	0	0	0	0	0	0
1.05 - 1.10	0	0	0	0	0	0
1.10 - 1.15	0	0	0	0	0	0
1.15 - 1.20	0	0	0	0	0	0
1.20 - 1.25	0	0	0	0	0	0
1.25 - 1.30	0	0	0	0	0	0
1.30 - 1.35	0	0	0	0	0	0
1.35 - 1.40	0	0	0	0	0	0
1.40 - 1.45	0	0	0	0	0	0
1.45 - 1.50	0	0	0	0	0	0
1.50 - 1.55	0	0	0	0	0	0
1.55 - 1.60	0	0	0	0	0	0
1.60 - 1.65	0	0	0	0	0	0
1.65 - 1.70	0	0	0	0	0	0
1.70 - 1.75	0	0	0	0	0	0
1.75 - 1.80	0	0	0	0	0	0
1.80 - 1.85	0	0	0	0	0	0

* End (of specimen)

† 0.05 in.(from end of specimen)

m Middle of specimen

TABLE 10

NUMBER OF PORES
DIMENSIONS: 2C, L

INTERVAL (mm)	FRACTURE SURFACE OBSERVATIONS	POLISHED DISK OBSERVATIONS 2*	2	49*	49†	49M
0.00 - 0.05	0	0	1	0	7	0
0.05 - 0.10	0	13	2	3	2	1
0.10 - 0.15	1	11	3	1	8	3
0.15 - 0.20	0	11	4	4	4	4
0.20 - 0.25	1	9	2	1	3	1
0.25 - 0.30	1	10	0	5	1	2
0.30 - 0.35	0	4	0	2	2	9
0.35 - 0.40	3	7	0	3	5	5
0.40 - 0.45	1	4	0	3	0	3
0.45 - 0.50	2	1	0	3	0	6
0.50 - 0.55	0	0	0	1	0	0
0.55 - 0.60	1	0	0	2	2	1
0.60 - 0.65	0	1	0	0	0	0
0.65 - 0.70	0	1	0	0	0	0
0.70 - 0.75	2	1	0	3	0	0
0.75 - 0.80	0	1	0	1	0	0
0.80 - 0.85	1	0	0	1	0	0
0.85 - 0.90	0	0	0	1	0	1
0.90 - 0.95	0	0	0	0	0	0
0.95 - 1.00	0	0	0	0	0	1
1.00 - 1.05	0	0	0	0	1	0
1.05 - 1.10	0	0	0	0	0	0
1.10 - 1.15	0	0	0	1	0	0
1.15 - 1.20	1	0	0	0	0	0
1.20 - 1.25	0	0	0	0	0	1
1.25 - 1.30	0	0	0	0	0	0
1.30 - 1.35	0	0	0	0	0	0
1.35 - 1.40	0	0	0	0	0	0
1.40 - 1.45	0	0	0	0	0	0
1.45 - 1.50	0	0	0	0	0	0
1.50 - 1.55	0	0	0	0	0	0
1.55 - 1.60	0	0	0	0	0	0
1.60 - 1.65	0	0	0	0	0	0
1.65 - 1.70	0	0	0	0	0	0
1.70 - 1.75	0	0	0	0	0	0
1.75 - 1.80	0	0	0	0	0	0
1.80 - 1.85	1	0	0	0	0	0

* End (of specimen)

† 0.05 in.(from end of specimen)

m Middle of specimen

TABLE 11

SAMPLE 7 *

NUMBER OF PORES WITH EQUIVALENT CIRCLE DIAMETER IN 0.025 mm INTERVALS

INTERVAL (mm)	NUMBER PORES WITH EQUIVALENT CIRCLE DIAMETER
0.025	28
0.075	11
0.125	2
0.175	2
0.225	2
Average	0.06
Std. Dev.	0.05

* General Motors sectioned and image analyzed sample 7.

TABLE 12

THE LARGEST DIMENSION, L (mm), OF WHITE REGIONS MEASURED FROM THE ENLARGED PRINT FROM THE RADIOGRAPHS

POLISHED SECTIONS OBSERVATIONS						
5	6	12*	14	26	49*	49m
2 @ 0.23	0.08	2 @ 0.15	0.15	12 @ 0.15	2 @ 0.23	3 @ 0.23
2 @ 0.38	2 @ 0.15	2 @ 0.23	3 @ 0.23	18 @ 0.23	2 @ 0.31	3 @ 0.31
2 @ 0.46	3 @ 0.31	3 @ 0.31	2 @ 0.31	5 @ 0.31	7 @ 0.38	9 @ 0.38
0.47	3 @ 0.38	3 @ 0.38	3 @ 0.38	5 @ 0.38	5 @ 0.46	5 @ 0.46
0.54	0.46	0.46	2 @ 0.46	2 @ 0.46	2 @ 0.54	5 @ 0.54
0.69	3 @ 0.54	0.54	3 @ 0.69	4 @ 0.54	3 @ 0.63	2 @ 0.62
0.77	2 @ 0.62		0.77	2 @ 0.77	0.69	2 @ 0.69
1.15	2 @ 0.69		0.92		0.77	0.77
	3 @ 0.77		1.08		0.85	0.92
	2 @ 0.92		1.30		2 @ 0.92	
	1.15		2 @ 1.54			
	1.69					

The total average of all the pores measured is 0.42 mm with a lower bound of 0.08 mm and an upper bound of 1.69 mm

* End (of specimen)

m Middle of specimen

@ X number of pores with the following dimension (i.e. 3 pores with length, 0.38 mm)

TABLE 13

MEASURED AREAL AND VOLUME FRACTION OF POROSITY

SAMPLE IDENTIFICATION	OPTICAL PHOTOGRAPHS AREAL FRACTION (%)
5	0.3
6	0.03
7†	0.6
11	0.1
12	0.05
12 END	0.5
14	0.3
16	0.3
26	0.3
49 MIDDLE	2.0
49 END	2.4
AVERAGE	0.63
STD. DEV.	0.08

† Analysis done by the General Motors Technical Center.

8. FIGURES

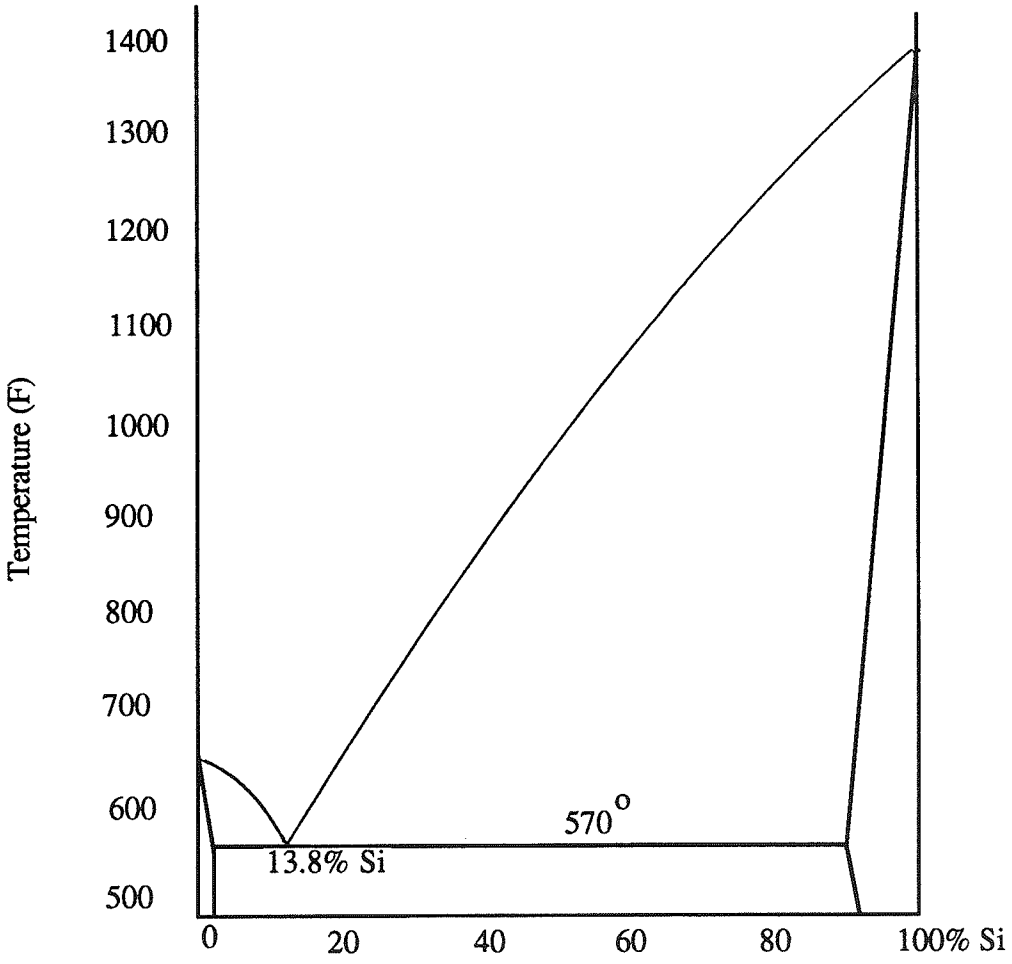

Figure 1 The Aluminum-Silicon phase diagram. The AlSi 319 alloy contains approximately 6 % silicon. [15].

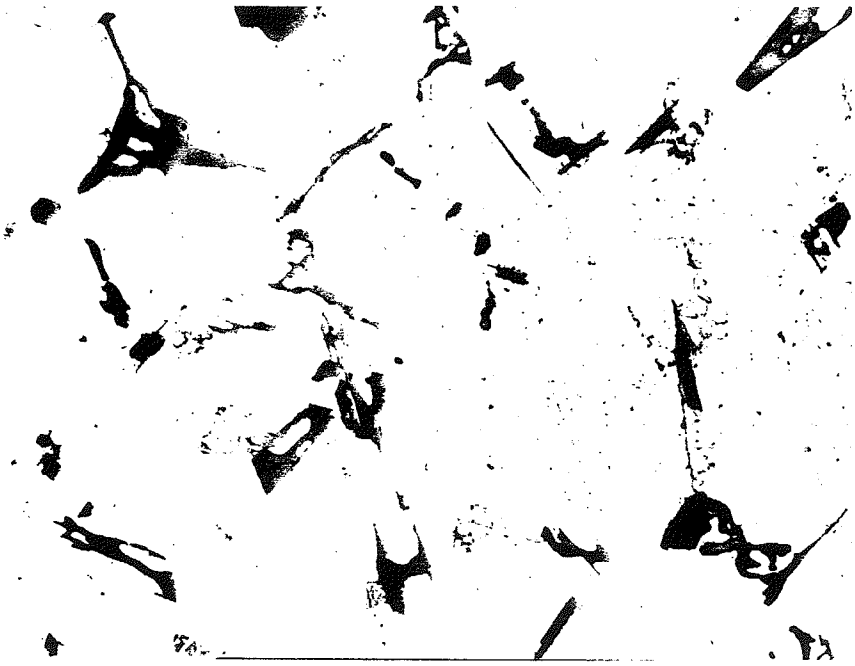

Figure 2 Photomicrograph of Aluminum-Silicon 319 Alloy (400X). The continuous phase is the alpha aluminum. The sharp gray particles are silicon. The medium gray blades are $Fe_2Si_2Al_9$. The black particles are Mg_2Si. The Light gray script is also known as 'Chinese Script' and are particles of $FeMg_3Si_6Al_8$. The dark gray, round particles are silicon eutectic. Keller's Etch

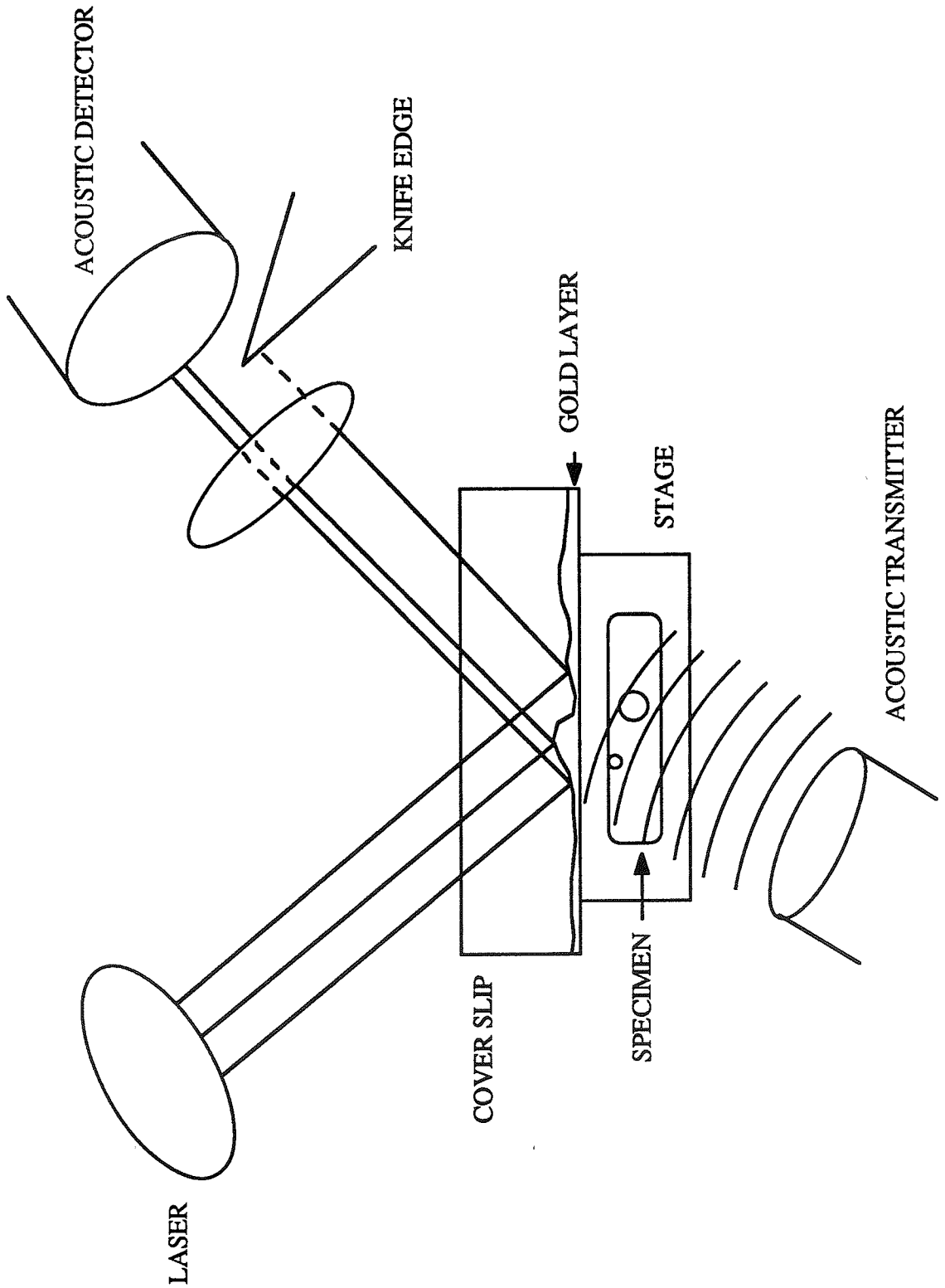

Fig. 3 Schematic diagram of the Acoustic Microscope.

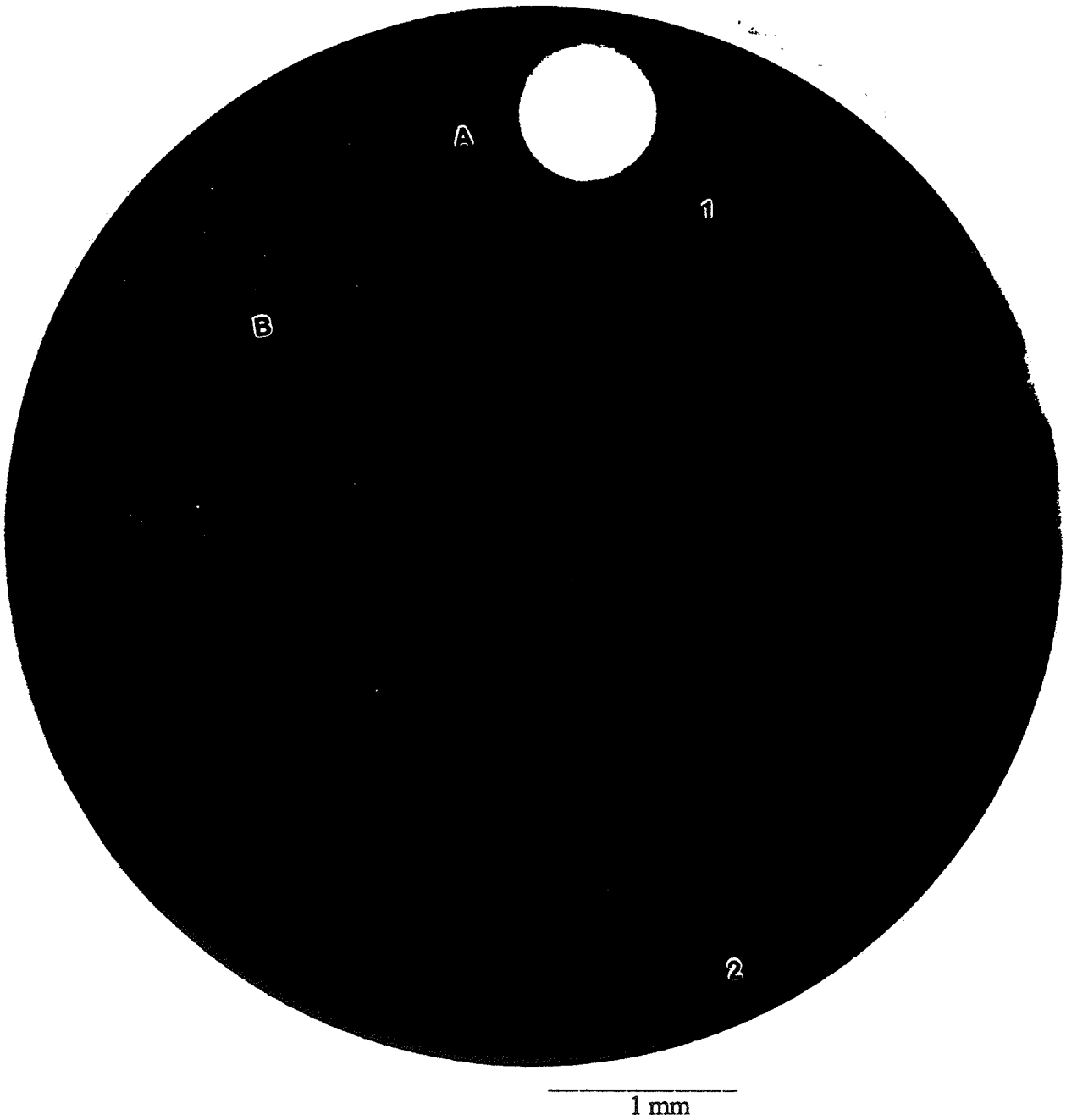

Figure 4 Enlarged photograph of the radiograph of polished section 49 End (30X). The porosity is seen as the white regions (as opposed to being observed as black regions on a radiograph due to the inverse nature of the photographic printing). Pores A and B are marked on the photograph. The pore marked 1 is an indication of a long and narrow pore and the pore marked 2 is an indication of a round pore.

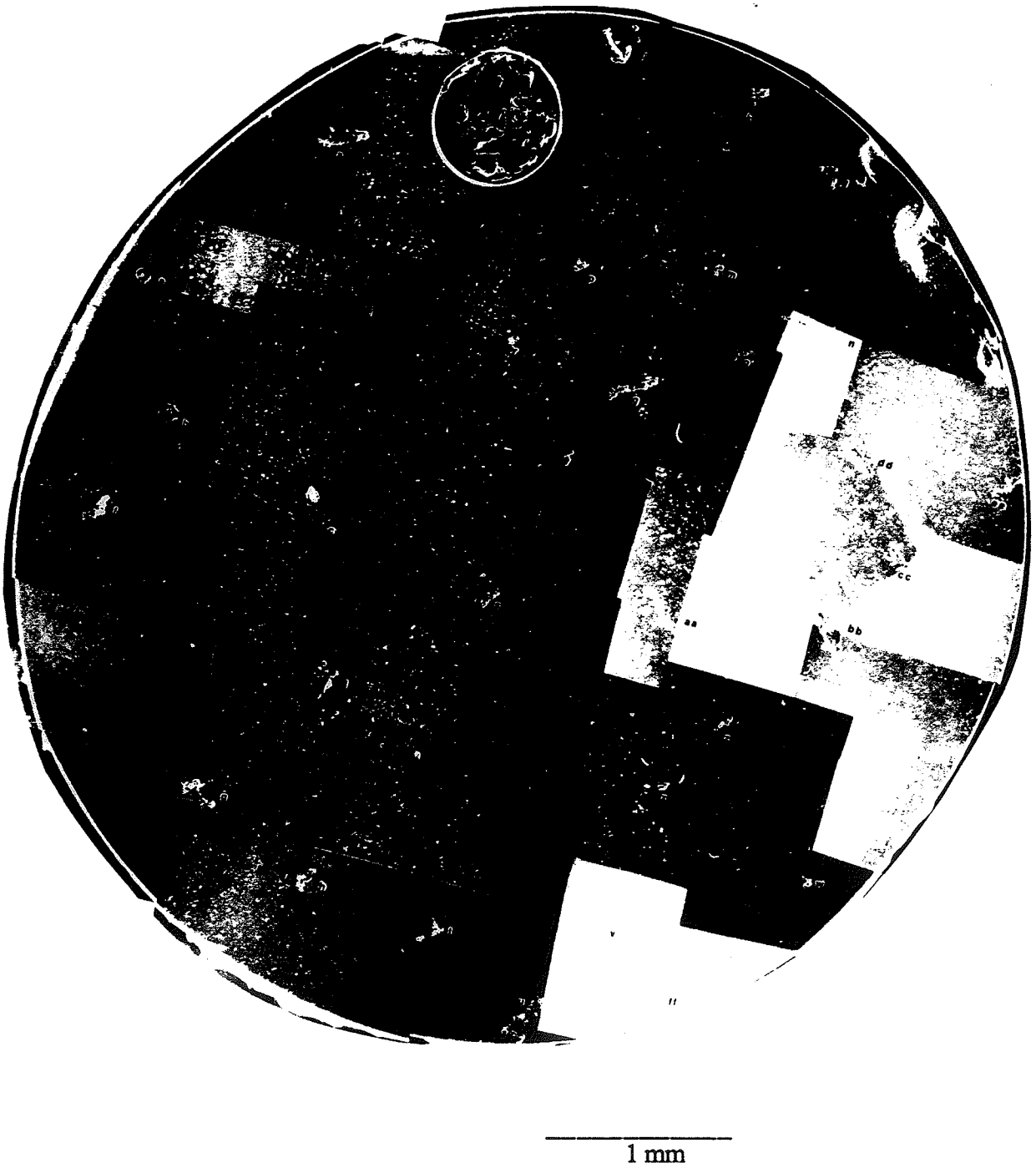

Figure 5 Montage of disk 49 End using the Scanning Electron Microscope (30X). The surface pores, A and B, are labelled on the montage.

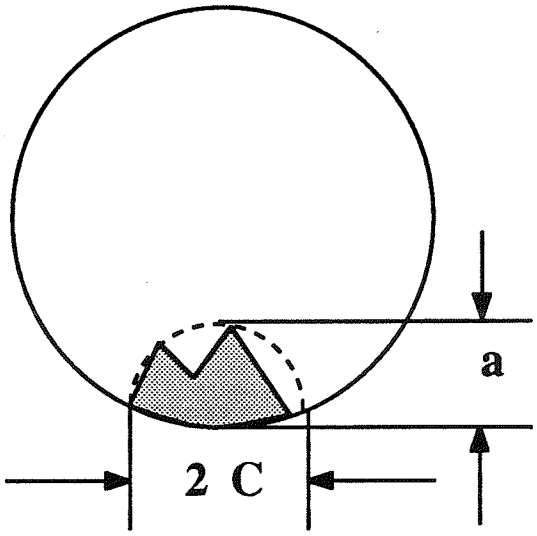

A

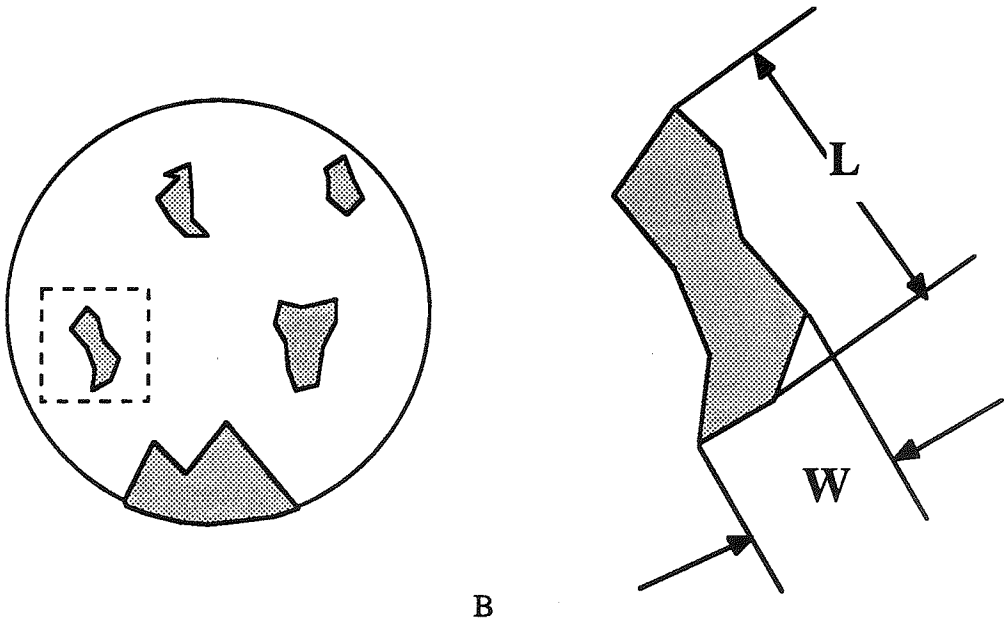

B

Figure 6 Schematic diagrams definining the dimensions measured.

A Schematic diagram of a surface initiation flaw in a failed fatigue sample.
B Schematic diagram of a polished section with several pores exposed.

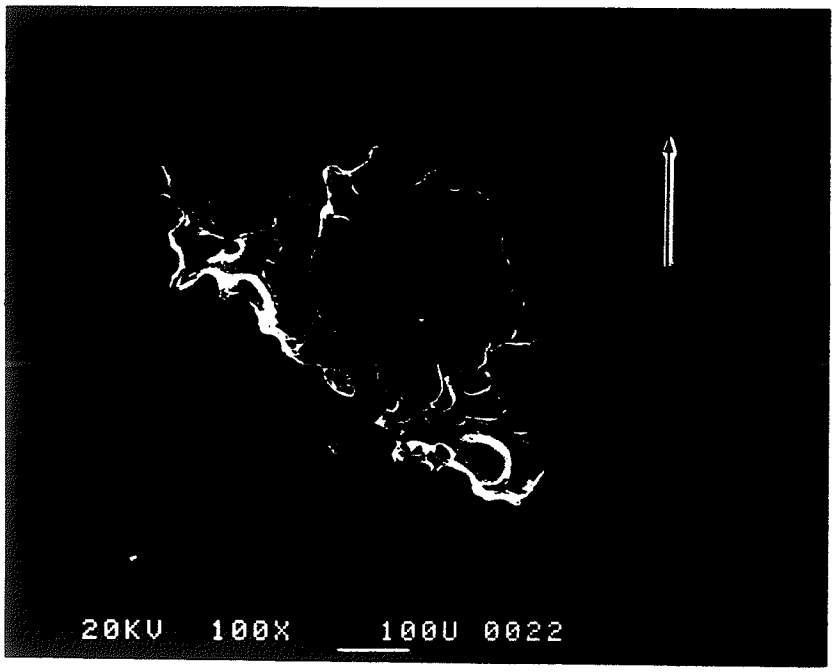

Figure 7 SEM photograph of pore A in polished section 49 End (100 X). The orientation of pore A of the SEM photograph with respect to the optical photograph is marked with an arrow and the letter, N.

Figure 8 SEM photograph of pore B in polished section 49 End (100 X)

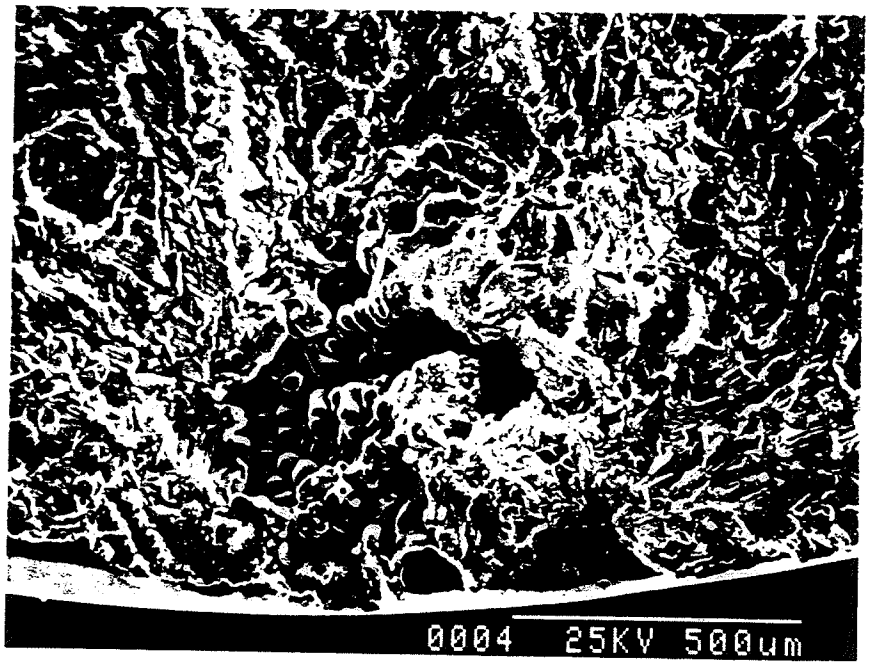

Figure 9 SEM image of pore initiating fatigue failure from Fatigue Sample 3 (78X)

Figure 10 Optical photograph of pore A in polished section 49 End (78 X) showing the silicon eutectic environment. The arrow and letter, N, marks the orientation of pore A of the optical photograph with respect to the SEM photograph.

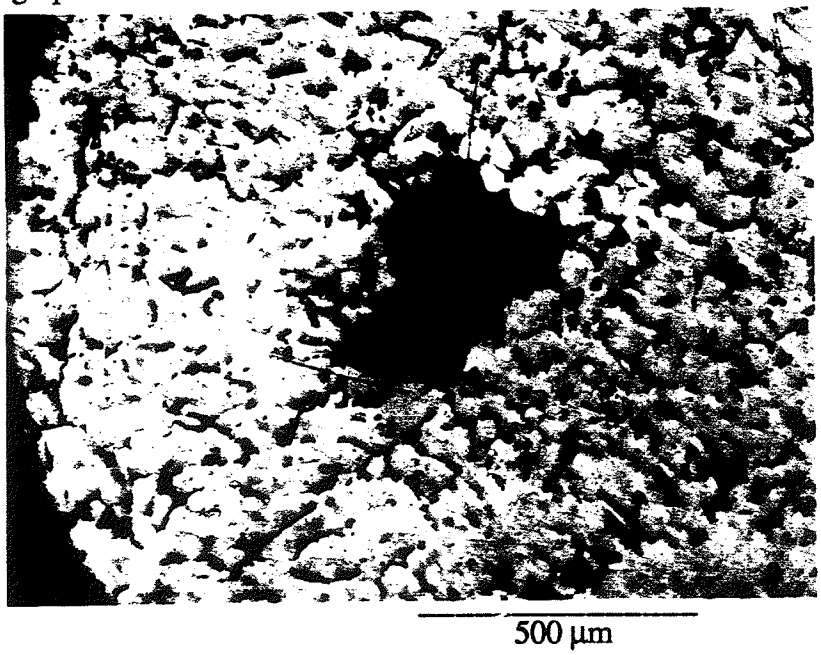

Figure 11 Optical photograph of pore B in polished section 49 End (78 X) showing the silicon eutectic environment.

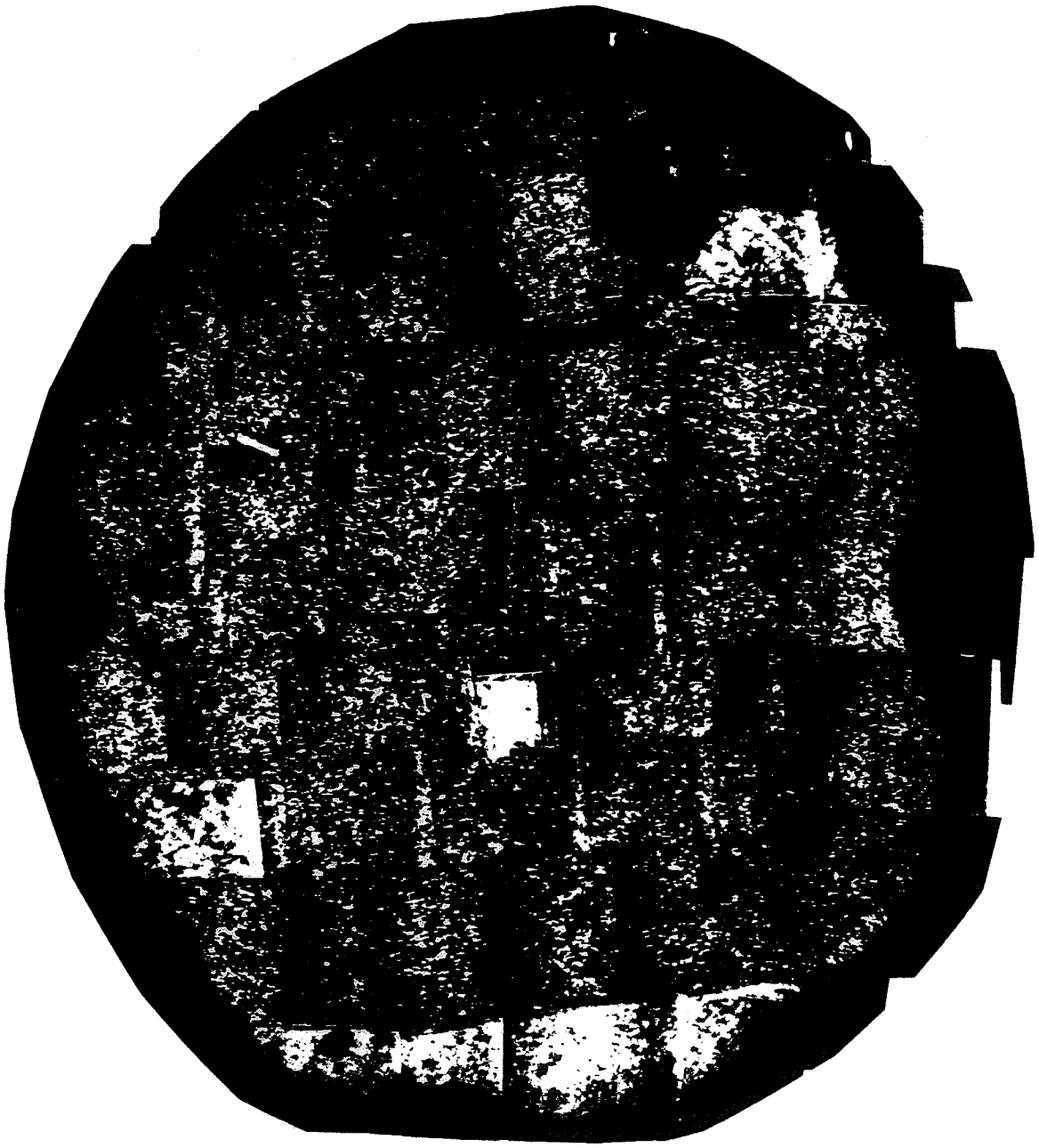

Figure 12 Montage of acoustical image of disk 49 End on the SLAM (10X).

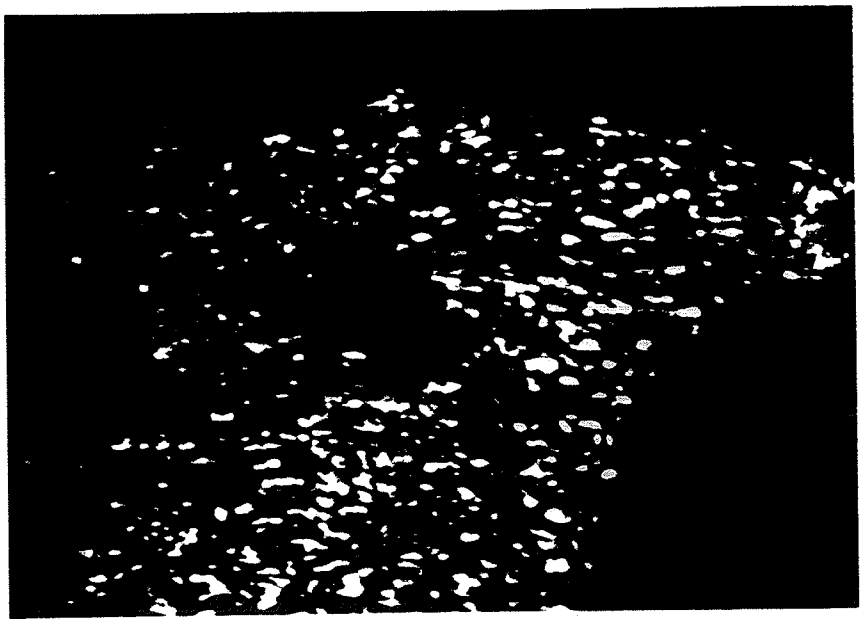

Figure 13 SLAM photograph of pore A in polished section 49 End (30 X) illustrating the acoustic patterns developed due to pores and the silicon eutectic.

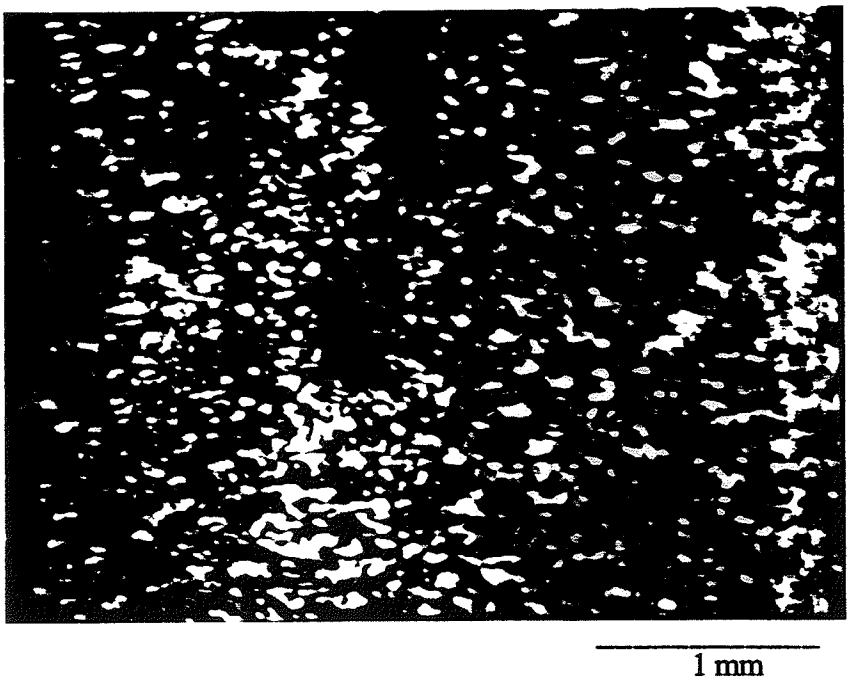

Figure 14 SLAM photograph of pore B in polished section 49 End (30 X) illustrating the acoustic patterns developed due to pores and the silicon eutectic.

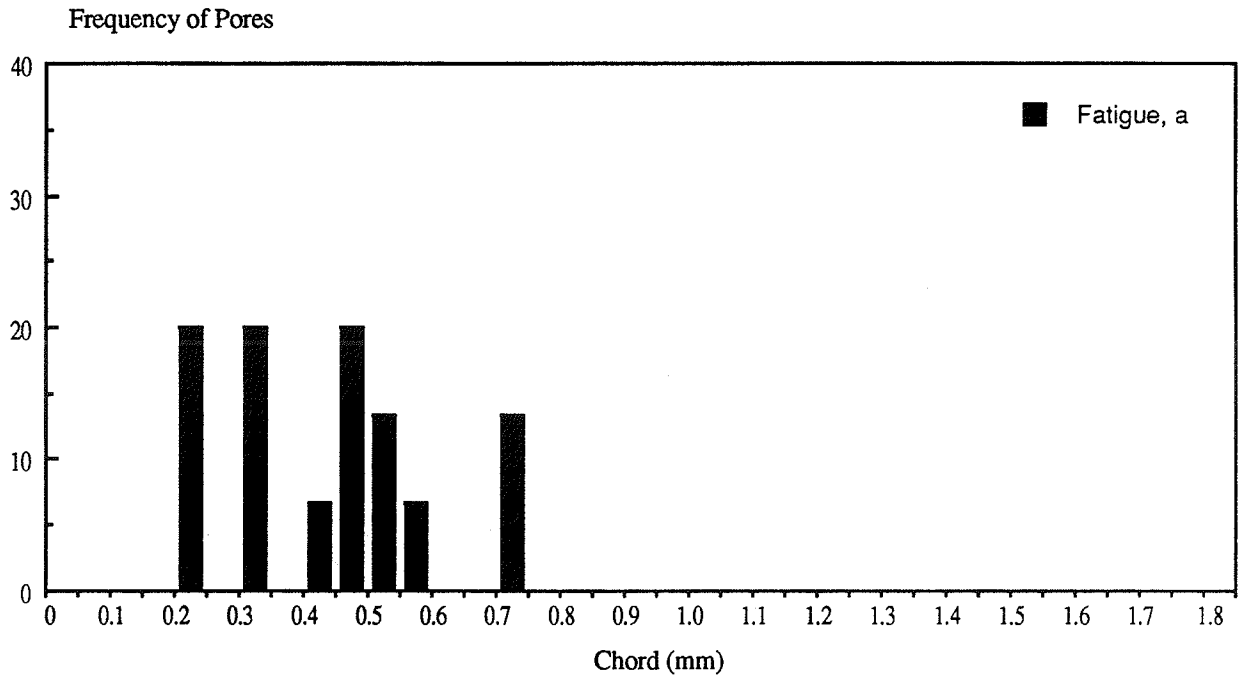

Figure 15 Histogram of the frequency of the dimension, a, of pores initiating fatigue failure. The average (a) is 0.43 with a lower bound of 0.20 and an upper bound of 0.75 mm.

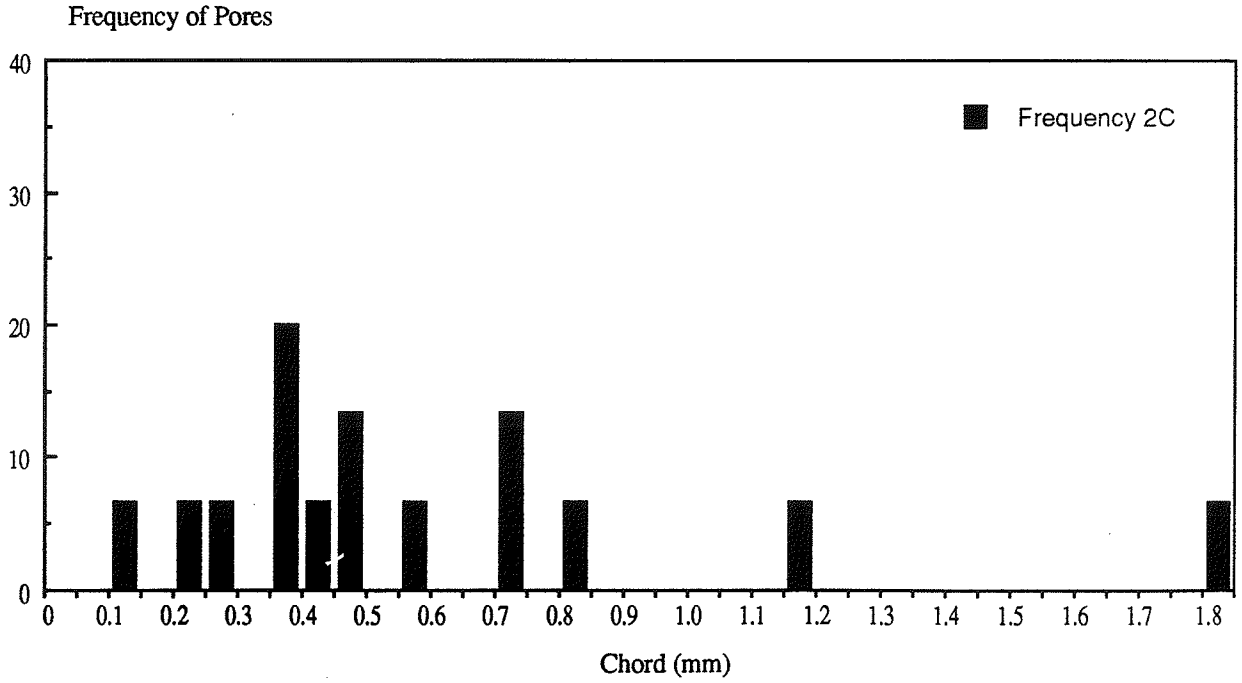

Figure 16 Histogram of the frequency of the dimension, 2C, of pores initiating fatigue failure. The average 2C is 0.58 with a lower bound of 0.10 and an upper bound of 1.85.

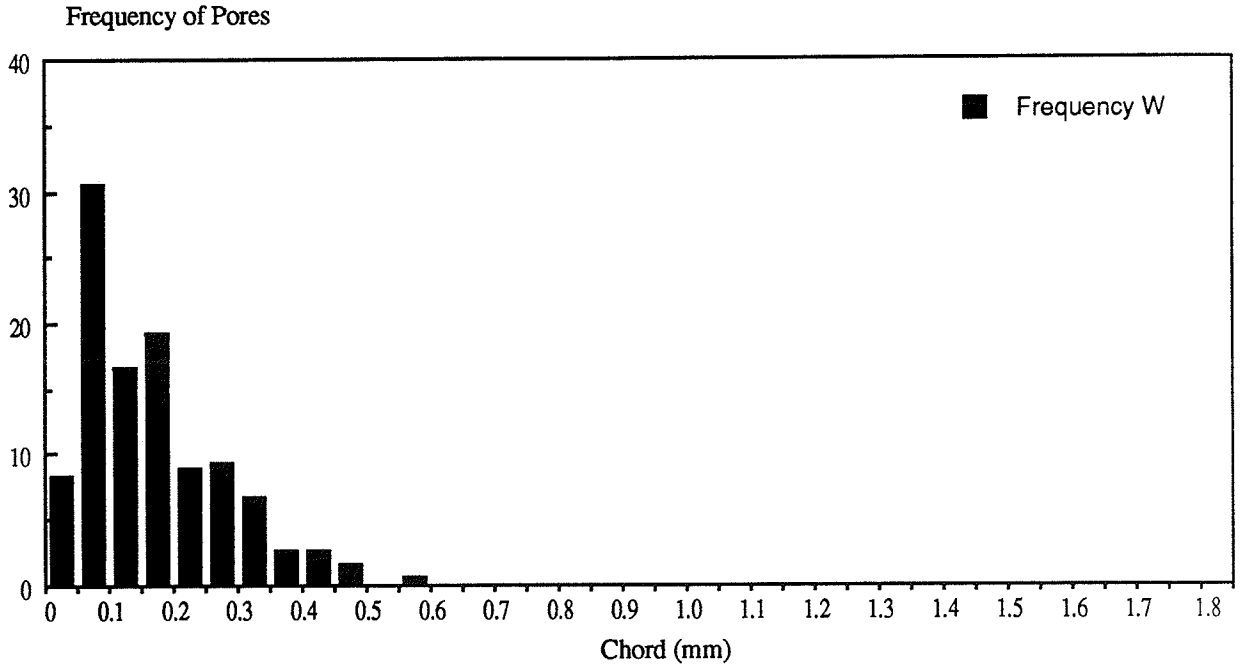

Figure 17 Frequency histogram of the dimension, W, of pores observed on the plane of polish. The average width, W, of the pores is 0.15 with a lower bound of 0.03 and an upper bound of 0.60 mm.

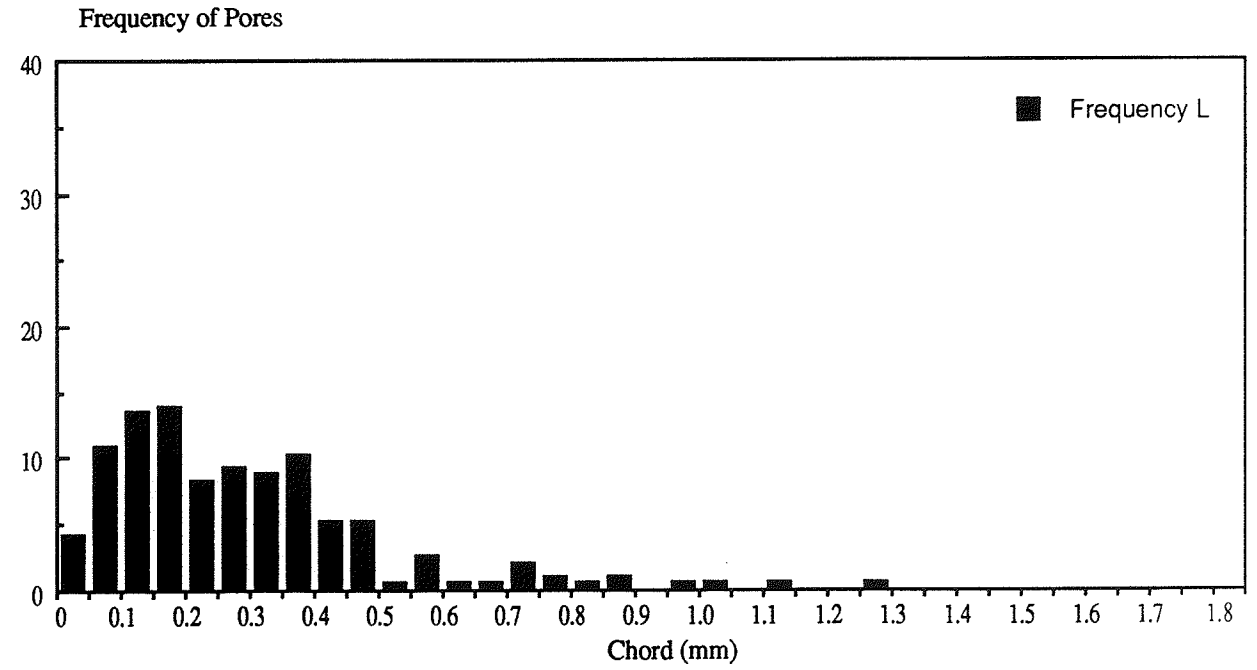

Figure 18 Frequency histogram of the dimension, L, of pores observed on the plane of polish. The average length, L, of the pores is 0.30 with a lower bound of 0.02 and an upper bound of 1.30 mm.

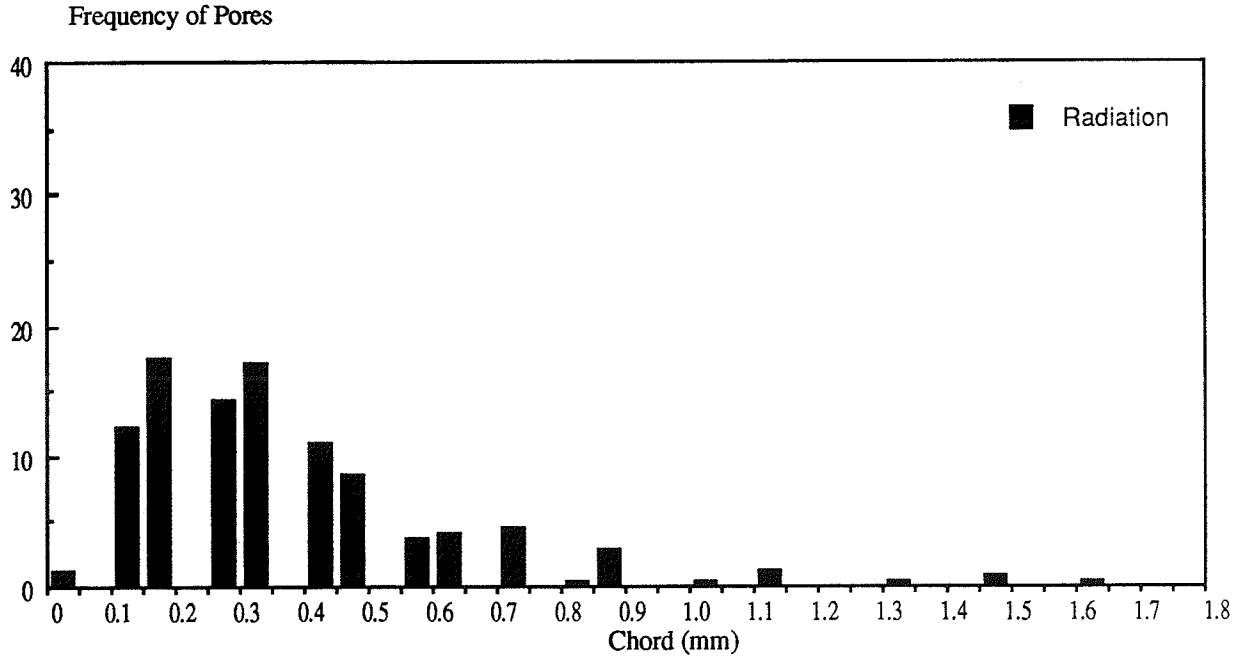

Figure 19 Histrogram of the frequency of the largest dimension observed on the radiographic print. The average length is 0.4 mm with a lower bound of 0.08 mm and an upper bound of 1.7 mm.

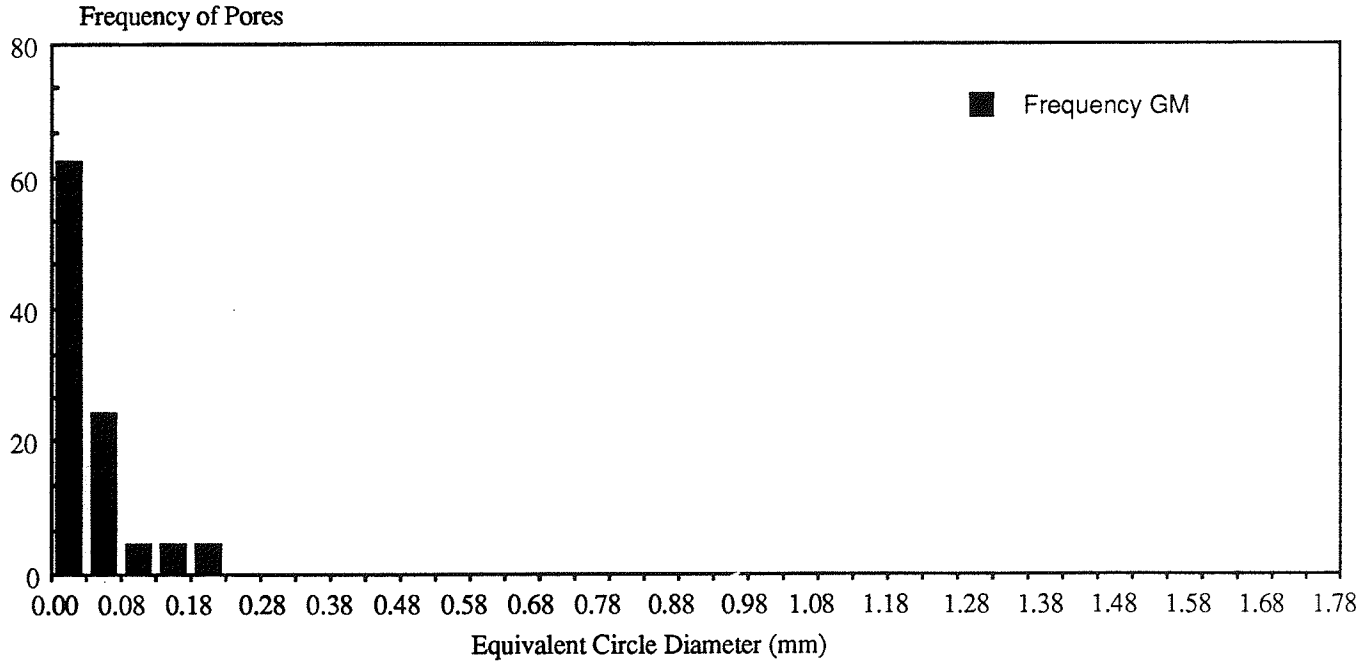

Figure 20 Histogram of the frequency of pores detected by an image analyzer at the General Motors Technical Center. The average diameter is 0.6 mm with a lower bound of 0.03 and upper bound of 0.23.

10/2/89

Dr. O'brien,

Here is a copy of my MS thesis. The xerox of the photographs did not reproduce very well - if you would like to see the details my officemate, Jason Ting (333 2749), has a complete (with original photographs) thesis.

Thank you for all your help!

Sincerely,

Kathy Holloway